8

Silicon-Based Third Generation Photovoltaics

Tetyana Nychyporuk and Mustapha Lemiti
University of Lyon, Nanotechnology Institute of Lyon (INL),
UMR CNRS 5270, INSA de Lyon,
France

1. Introduction

In order to ensure the widespread use of photovoltaic (PV) technology for terrestrial applications, the cost per watt must be significantly lower than 1$ / Watt level. Actually, the wafer based Silicon (Si) solar cells referred also as the 1st generation solar cells are the most mature technology on PV market. However such PV devices are material and energy intensive with conversion efficiencies which do not exceed in average 16 %. In 2008 the average cost of industrial 1 Wp Si solar cell with conversion efficiency of 14.5 % (multicrystalline Si cell of 150 x 150 mm^2, 220 μm of thick, SiN antireflecting coating with back surface field and screen printing contacts) achieved approximately 2.1 € assuming the production volume of 30 – 50 M Wp / per year (Sinke et al., 2008). At that cost level, the PV electricity still remains more expensive comparing with traditional nuclear or thermal power engineering. One of the most promising strategies for lowering PV costs is the use of thin film technology, referred also as 2nd generation solar cells. It involves low cost and low energy intensity deposition techniques of PV material onto inexpensive large area low-cost substrates. Such processes can bring costs down but because of the defects inherent in the lower quality processing methods, have reduced efficiencies compared to the 1st generation solar cells.
Material limitations of the 1st generation solar cells and efficiency limitations of the 2nd generation solar cells are initiated boring of the Si-based 3rd generation photovoltaic. Its main goal is to significantly increase the conversion efficiency of low-cost photovoltaic product. Indeed, the Carnot limit on the conversion of sunlight to electricity is 95% as opposed to the theoretical upper limit of 30% for a standard solar cell (Shockley & Queisser 1961). This suggests the performance of solar cells could be improved 2 – 3 times if different concepts permitting to reduce the power losses were used.
The two most important power loss mechanisms in single-band gap photovoltaic cells are *(1)* the inability to absorb photons with energy less than the band gap and *(2)* thermalisation of photon energy exceeding the gap (Fig. 1). Longer wavelength is not absorbed by the solar cell material. Shorter wavelength generates an electron-hole pair greater than the bandgap of the p-n junction material. The excess of energy is lost as heat because the electron (hole) relaxes to the conduction (valence) band edges. The amounts of the losses are around 23 % and 33 % of the incoming solar energy, respectively (Nelson, 2003). Other losses are junction loss, contact loss and the recombination loss. Theory predicts (Shockley & Queisser 1961) that the highest single – junction solar cell efficiency is roughly 30%, assuming such factors as the intensity of one sun (no sunlight concentration), a one-junction solar cell (a single material with a single bandgap), and one electron-hole pair produced from each incoming photon.

To efficiently convert the whole solar spectrum into the electricity three main families of approaches have been proposed (Green et al., 2005) (Green, 2002): *(i)* increasing the number of bandgaps (*tandem cell* concept); *(ii)* capturing carriers before thermalisation, and *(iii)* multiple carrier pair generation per high energy photon or single carrier pair generation with multiple low energy photons. Up to now, tandem or in other words multijunction cells provide the best-known example of such high-efficiency approaches. Indeed, the loss process *(2)* of Fig. 1 can be largely eliminated if the energy of the absorbed photon is just a little higher that the cell bandgap. The concept of tandem solar cells is based on the use of several solar cells (or subcells) of different bandgaps stacked on top of each other (Fig. 2), with the highest bandgap cell uppermost and lowest on the bottom. The incident light is automatically filtered as it passes through the stack. Each cell absorbs the light that it can most efficiently convert, with the rest passing through to underlying lower bandgap cells (Green et al., 2007). The using of multiple subcells in the tandem cell structure permits to divide the broad solar spectrum on smaller sections, each of which can be converted to electricity more efficiently. Performance increases as the number of subcells increases, with the direct sunlight conversion efficiency of 86.8 % calculated for an infinite stack of independently operated subcells (Marti & Araujo, 1996). The efficiency limit reaches 42.5 % and 47.5 % for 2- and 3-subcell tandem solar cells (Nelson, 2003) as compared to 30% of one junction solar cell.

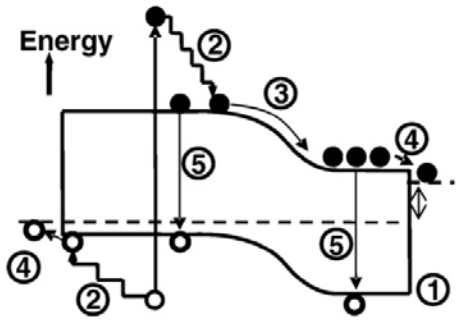

Fig. 1. Loss processes in a standard solar cell: *(1)* non-absorption of below band gap photons; *(2)* lattice thermalisation loss; *(3)* and *(4)* junction and contact voltage losses; *(5)* recombination loss (Green, 2003).

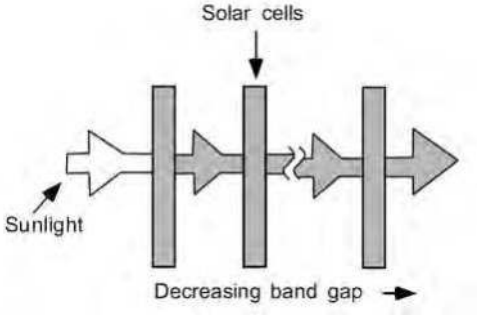

Fig. 2. Tandem cell approach (Green, 2003).

Having to independently operate each subcell is a complication best avoided. Usually, subcells are designed with their current output matched so that they can be connected in series. This constrain reduces performance. Moreover, it makes the design very sensitive to the spectral content of the sunlight. Once the output current of one subcell in a series connection drops more than about 5 % below that of the next worst, the best for overall performance is to short-circuit the low-output subcell, otherwise it will consume, rather than generate power.

It should be also noted the common point of confusion about solar cells efficiency. The measured efficiency of solar cell depends on the spectrum of its light source. The space solar

spectrum or air mass zero (AM0) spectrum is richer in ultraviolet light than the typical terrestrial solar spectrum (air mass 1.5 or AM1.5). Taking into account that the ultraviolet light is converted into electricity less efficiently than the other parts of the spectrum, the resulting efficiencies for AM0 are thus lower (Green et al., 2010). Since cells are typically measured under the spectrum for their intended use and efficiencies are not easily converted, this chapter will indicate efficiencies measured under non-concentrated AM1.5 at 25° unless otherwise specified.

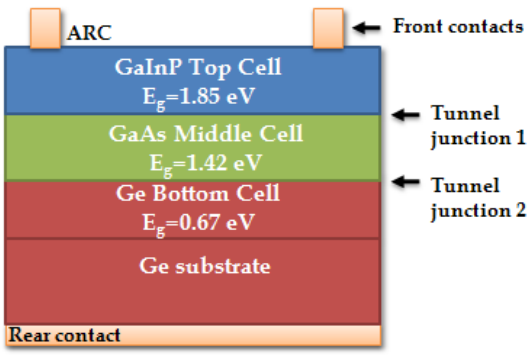

Fig. 3. Schematic view of GaInP/GaAs/Ge solar cell.

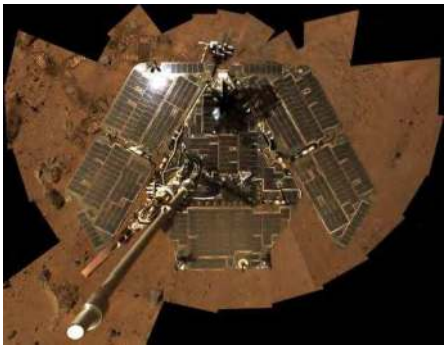

Fig. 4. Using of multijunction solar cells for Mars rover missions [1].

Up today the tandem cells have been developing on monolithic integration of non-abundant III –V materials by means of rather expensive technologies of fabrication like molecular beam epitaxy (MBE) or metal-organic chemical vapor deposition (MOCVD). Currently commercially available multijunction cells consist of three subcells (GaInP/GaAs/Ge), which all have the same lattice parameter and are grown in a monolithic stack (Fig. 3). The subcells in this monolithic stack are series connected through the tunnel junctions. The record efficiency of 32% was achieved in 2010 for this type of cells (Green et al., 2010). These high-efficiency solar cells are being increasingly used in solar concentrator systems, where development of both the solar cells and the associated optical and thermal control elements are actively being pursued. The performance of tandem solar cells has been demonstrated, but work is continuing to increase the numbers of junctions and optimize the bandgap junctions. The choice of materials with optimal or near-optimal bandgap is severely limited by the lattice matching constraint of these cells. Another approach to increasing of multijunction solar cell efficiency is the incorporation of materials with a mismatch in the lattice constant. Graded composition buffers between the lattice mismatched subcells are used to reduce the density of the threaded dislocations resulting from the lattice mismatch strain. Lattice mismatch technology opens the parameter space for junction materials, allowing the choice of materials with more optimal bandgaps and a potential for higher cell efficiency.

[1] http://marsrovers.nasa.gov/gallery/press/spirit/20060104a.html

In 2010 the cost of multijunction solar cells still remains too high to allow their use outside of specified applications (for example space applications, Mars rover missions (Crisp et al., 2004) (Fig. 4)…). The high cost is mainly due to the complex structure and the high price of materials. In this context the fabrication of multijunction solar cells on the base of abundant low-cost materials that do not cause toxicity in the environment and by using approaches amenable to large scale mass production, like thin film deposition techniques, remains challenging.

2. Silicon based tandem cells

Silicon is a benign readily available material, which is widely used for solar cell fabrication. It has a bandgap of 1.12 eV at 300 K, which is close to optimal not only for standard, single p – n junction cell, but also for the bottom cell in a 2-cell or even a 3-cell tandem stack (Conibeer et al., 2008). Therefore a solar cell entirely based of Si and its dielectric compounds (referred also as *all-Si tandem solar cell*) with other abundant elements (i. e. silicon dioxide, nitrides or carbides) fabricated with thin film techniques, is advantageous in terms of potential for large scale manufacturing and in long term availability of its constituents. As was already mentioned previously, thin film low-temperature deposition techniques results in high defect density films. Hence solar cells must be thin enough to limit recombination due to their short diffusion lengths, which in turn means they must have high absorption coefficients.

For AM1.5 solar spectrum the optimal bandgap of the top cell required to maximize conversion efficiency is ~1.7 to 1.8 eV for a 2-cell tandem with a Si bottom cell and 1.5 eV and 2.0 eV for the middle and upper cells for a 3-cell tandem (Meillaud et al., 2006). It should be also noted that for terrestrial applications (AM1.5 solar spectrum), the highest bandgap necessary for the Si-based tandem solar cells is limited to 3.1 eV, the energy at which the absorption from the encapsulation material, such as ethylene-vinyl acetate (EVA), starts to play an important role.

2.1 Quantum confinement in Si nanostructures

To increase Si bangap, nanoscale size dependent quantum confinement effect can be used. Indeed, the quantum confinement effect manifests itself by significant modification of electronic band structure of Si nanocrystals when their size is reduced to below the exciton Bohr radius (~4.9 nm) of bulk Si crystals. In particular, quantum confinement effect provokes the increasing of the effective bandgap of Si nanocrystals. Moreover, for indirect bandgap semiconductors, like Si, geometrical confinement of carriers increases the overlap of electron and hole wavefunctions in momentum space and thus enhances the oscillator strength and as a consequence increases its absorption coefficient. From this effect, one can expect Si nanocrystals to behave as direct bandgap semiconductors. However, there is some evidence suggesting that the momentum conservation rule is only partially broken and Si nanocrystal strongly preserves the indirect bandgap nature of bulk Si crystals (Kovalev et al., 1999). Si nanostructures are thus the perfect candidates for higher bandgap materials in all-Si tandem cell approach.

Since the observation in 1990 of strong room-temperature photoluminescence from nanostructured porous Si (Canham, 1990), significant scientific interest has been focused of the simulation of optical and electrical properties of Si nanostructures regarding their size, shape, surface termination, number and degree of interconnections, impurity doping and so

on. Many reviews addressing this problematic since appeared (one of the good recent reviews is Ref (Bulutay & Ossicini, 2010)). In this paragraph we will only underline some important points resulting from quantum confinement effect.
Ab initio calculations using density functional theory (DFT) indicate that the increasing of the optical bandgap of Si nanocrystals (or in other words quantum dots (QDs)) is expected to vary from 1.4 to 2.4 eV for a nanocrystal size of 8-2.5 nm (Ögüt et al., 1997). However, further DFT calculations have found that in addition to quantum confinement effect in small QDs, the matrix has a strong influence of the resulting energy levels (König et al., 2009). With increasing polarity of the bonds between the nanocrystal and the matrix, there is an increasing dominance of the interface strain over quantum confinement. For a 2 nm diameter nanocrystal, this strain is such that the highest occupied molecular orbital (HOMO)-lowest unoccupied molecular orbital (LUMO) gap is significantly reduced in a polar SiO_2 matrix but not much affected in a less polar SiN_x or nonpolar SiC matrix (König et al., 2009). It is also shown the reduction in gap energy on going from a QD in vacuum to the one embedded in a dielectric. An additional freedom of material design can be also introduced by impurity doping and interconnections between Si QDs, the both ones modify its optical and electrical transport properties (Nychyporuk et al., 2009) (Mimura et al., 1999).

3. Silicon quantum dot solar cells

Si QDs offer the potential to tune the effective bandgap, through quantum confinement, and allow fabrication of optimized tandem devices in one growth run in a thin film process.

3.1 Fabrication of Si QD nanostructures

Different technological approaches allowing formation of Si quantum dots in a dielectric matrix have already been developed, permitting to obtain Si nanocrystals as small as 1 nm in diameter. Between the most used deposition techniques one can cite reactive evaporation, ion implantation, sputtering and plasma enhanced chemical vapor deposition (PECVD). Considerable work has been done on the growth of Si nanocrystals embedded in silicon oxide dielectric matrices (SiO_2) (Zacharias et al., 2002) (Stegemann et al., 2010), silicon nitride (Si_3N_4) (Kim et al., 2006) (Cho et al., 2005) (Mercaldo et al., 2010) (So et al., 2010) and silicon carbide (SiC) (Song et al., 2008) (Kurokawa et al., 2006) (Gradmann et al., 2010) (Löper et al., 2010) (Cho et al., 2007). An accurate control of the size and density of Si nanocrystals is mandatory in bandgap engineering for solar cell applications. It should be noted that Si nanocrystals prepared by different methods present slightly different properties which depend on the preparation procedure, because of different defect density, different degree of interconnections between the nanocrystals, different surface termination, and so on.
Conventionally, Si QDs in dielectric matrix like SiO_2, Si_3N_4 and SiC can be synthetized by self-organized growth from Si rich dielectric layers, which are thermodynamically unstable and therefore undergo phase separation upon appropriate post-annealing step to form nanocrystals. For example for Si rich oxide layer, the precipitation occurs according to the following:

$$SiO_x \rightarrow \frac{x}{2} SiO_2 + \left(1 - \frac{x}{2}\right) Si$$

It should be noted that due to the fact that both the polarity and length of the bonds decrease towards those of Si-Si for SiO_2 to Si_3N_4 and SiC, this implies that the segregation

and precipitation effect for Si in the three matrices would decrease such that in SiC formation of QDs is likely to be most difficult.

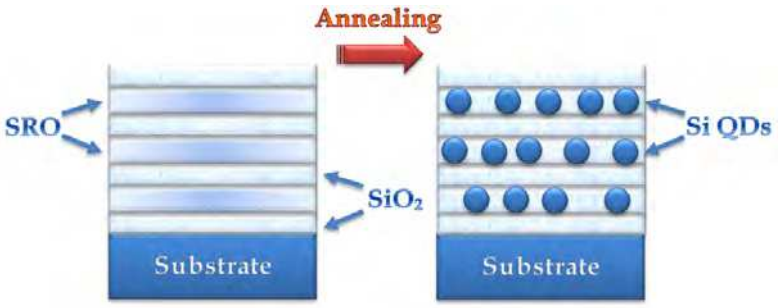

(a)

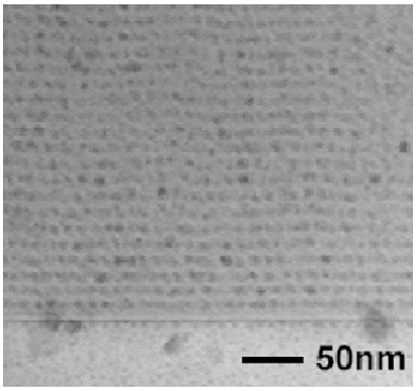

(b)

Fig. 5. (a) Multi-layer structure illustrating precipitation of Si QDs in a Si-rich layer; (b) TEM image of a superlattice of Si QDs in SiO_2 matrix (Conibeer et al., 2008).

The QD size and density control are normally realized by changing the chemical stoichiometry of the bulk films. By reducing the Si-richness in a bulk Si-based matrix, smaller nanocrystals can be achieved. Nevertheless, this will simultaneously reduce the density of nanocrystals in the film due to the reduced Si-richness. The low density of QDs with desired size leads to a negative effect on the electrical conductivity of the films. Moreover, the assumption that all the excess Si precipitates to nanocrystals turns out to be oversimplification. In fact, it has been observed that only half the excess Si clusters in these precipitates upon annealing at 1000°C for 30 min, in material deposited by PECVD, with a considerable amount of suboxide material forming in the matrix. Therefore, the method allowing a fabrication of high density, but narrow size distributed Si QDs films via superlattice approach, firstly reported by Zacharias (Zacharias et al., 2002) , was adopted by the majority of researchers. It should be mentioned that even without using the multilayer

approach it is still possible to fabricate well – ordered and uniform Si nanocrystals in a film with a high dot density (Surana et al., 2010).

3.1.1 Si QDs in silicon oxide matrix

A simple technique to prepare the multilayer structure known also as superlattices of Si QDs in silicon oxide matrix was firstly reported by Zacharias (Zacharias et al., 2002) . It consists in deposition of alternating layers of stoichometric Si oxide (SiO_2) and Si rich oxide (SRO) of thicknesses down to 2 nm. This precision is normally achieved by using RF magnetron sputtering or plasma enhanced chemical vapor deposition (PECVD) technique. The deposition consisting typically of 20-50 bi-layers is followed by the annealing step is N_2 ambient from 1050 to 1150°C for 1 h. During the annealing step, the surface energy minimization favors the precipitation of Si in the SRO layer into approximately spherical QDs (Conibeer et al., 2008). This process is illustrated on Fig. 5 (a). The diameter of Si QDs is constrained by the SRO layer thickness and quite uniform size dispersion is achieved within about 10% (Zacharias et al., 2002) . The density of the QDs can be varied by the composition of the SRO layer. Fig. 5 (b) shows typical transmission electron microscope (TEM) of the multi-structure SiQDs in SiO_2 matrix grown by this method. TEM evidence indicates that these nanocrystals tend to be spherical – as surface energy minimization would dictate - and at this scale would have energy levels confined in all three dimensions and hence can be considered as quantum dots.

Nowadays, the phase separation, solid state crystallization and optical properties of $SiO_2/SRO/SiO_2$ superlattices are already well understood. However, it is a major challenge to achieve charge carrier transport through a network of Si QDs embedded in a SiO_2 matrix. Therefore, other Si based host matrices such as Si_3N_4 or SiC that feature lower energy band offsets with respect to the Si band edges and thus higher carrier mobility are attractive.

3.1.2 Si QDs in silicon nitride matrix

For the reasons stated above, it was explored the fabrication of Si QDs in silicon nitride matrix. Thick layers of silicon-rich nitride, when annealed at above 1000°C, precipitate to Si QD (Kim et al., 2005). Multilayered structures also result in Si QD formation with controlled size of the Si QDs (Cho et al., 2005). The annealing temperature can also be used to modify the nitride matrix, with it being amorphous below 1150°C but with crystalline nitride phases, in addition to the Si QDs, appearing at temperatures ranging from 1150 to 1200° (Scardera et al., 2008). Multilayered structures can be deposited by sputtering or by PECVD with growth parameters and annealing conditions very similar to those for oxide giving good control of QD sizes. The main difference is the extra H incorporation with PECVD that requires an initial low-temperature anneal to drive off excess hydrogen and prevent bubble formation during the high-temperature anneal (Cho et al., 2005).

Si QDs can also be grown *in situ* during PECVD deposition, where they form in the gas phase (Lelièvre et al., 2006). There is much less control over size and shape but no high-temperature anneal is required to form the Si QDs (Fig. 6 (a)). Multilayer growth using this *in-situ* technique has also been attempted with irregular shaped but reasonably uniform sized Si QDs (Fig. 6 (b)).

The formation of Si quantum dots in SiO_2/Si_3N_4 hybrid matrix was also reported (Di et al., 2010). In this approach alternating silicon rich oxide and Si_3N_4 layers were produced followed by post-deposition anneals. In addition, it should be noted that Si_3N_4 acts as a better diffusion barrier compared to SiO_2. It restricts the displacement of Si atoms as well as dopant atoms under high processing temperatures.

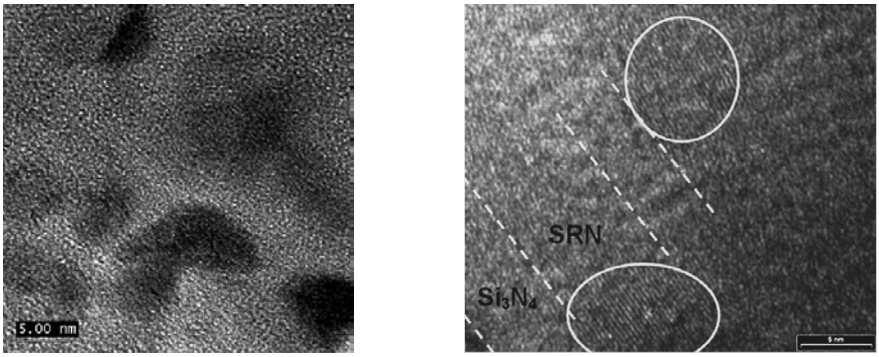

(a) (b)

Fig. 6. *In-situ* grown Si QDs in the gas phase and dispersed in Si_3N_4 matrix: (a) One layer structure (Lelièvre et al., 2006); (b) multi-layer structure (Conibeer et al., 2008).

3.1.3 Si QDs in silicon carbide matrix

Si QDs in a SiC matrix offer an even lower barrier height and hence potentially better electronic transport properties. However, the low barrier height also limits the minimum size of QDs to about 3 nm or else the quantum-confined levels are likely to rise above the level of the barrier, which should be around 2.3 eV for amorphous SiC. Si QDs in SiC matrix have been formed in a single thick layer by Si-rich carbide deposition followed by high-temperature annealing at between 800° and 1100°C in a very similar process to that for oxide (Fig. 7). $Si_{1-x}C_x$/SiC multilayers have also been deposited by sputtering to give better control over the Si QD as with oxide and nitride matrices. However, contrary to these previous matrices, the both Si and SiC QDs have been produced by high temperature annealing of Si –rich SiC layer or in a $SiC_{1-x}C_x$/SiC multistructure. The formation of SiC nanocrystals can hinder the formation of Si QDs.

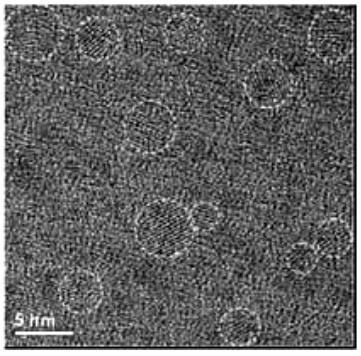

Fig. 7. Cross-sectional HRTEM image of Si-rich SiC layer after the thermal annealing (Conibeer, 2010).

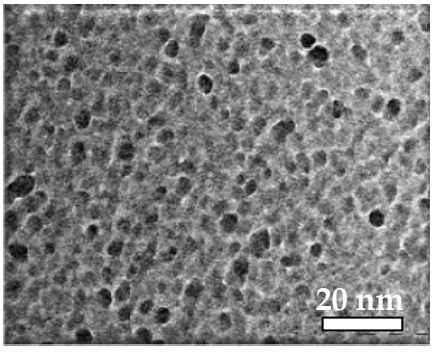

Fig. 8. TEM image interconnected Si QDs forming thin films.

3.1.4 Interconnected Si QDs forming thin films

To be successfully applied as a material for all-Si tandem solar cells, the small size of Si QDs is not the single prerequisite. It is also necessary to assure their high density in order to achieve a direct tunneling of the photogenerated charge carriers between the QDs. This still constitutes the bottleneck of the approaches cited above. Recently, the fabrication of thin films composed by highly packed Si QDs with a controlled bandgap values was reported (Nychyporuk et al., 2009). This approach is based on the *in-situ* nucleation of Si QDs in the gas phase during PECVD deposition by using SiH_4 as a gas precursor. Indeed, the dust particle formation in Ar-SiH_4 plasma is known to be a time-dependent four step process occurring in the gas phase: *(i)* polymerization phase, *(ii)* accumulation phase, *(ii)* coalescence and *(iv)* surface deposition growth. During the polymerization phase, the nucleation of extremely small particles (~1 nm) takes place. They progressively grow in size with time and at the end of the polymerization phase, starting from about 1 nm, a short accumulation phase begins. During this phase the nanoparticles size remains constant and only their density increases in the plasma environment. The coalescence phase starts once the nanoparticles critical density is reached. The small nanoparticles (~1 nm) begin to agglomerate at least two by two to form larger nanoclusters. In consequence, a number of interconnections between the nanoparticles increases. The final phase corresponds to the plasma species deposition on the surface of strongly agglomerated nanoparticles. During this phase a hydrogenated amorphous Si shell layer is formed around the crystalline Si core. The thickness of this amorphous shell increases with time. The square wave modulation of the power amplitude applied to the plasma has been found as a suitable technique permitting to obtain the deposition of Si QDs with required size. It consists of alternating periods of plasma switching time followed by the plasma extinction time. As a result, Si QDs grown in the gas phase during the plasma switching time were deposited on a substrate (Fig. 8). The careful tuning of the plasma switching time permits to precisely control the phase of Si QD growth and as a consequence their size and degree of interconnections between them. Si QD based thin films deposited under dusty plasma conditions appear to be promising candidates for all-Si tandem solar cell applications.

3.2 Shallow-impurity doped Si nanostructures

A requirement for a tandem cell element is the presence of some form of junction for carrier separation. Phosphorous (P) and boron (B) are excellent dopants in bulk Si as they have a high solid solubility and alter the conductivity of the bulk Si by several orders of magnitude. Hence they are good initial choices to study the doping in the Si nanocrystals.

Doping of Si nanostructures is a subject of intense research (Tsu et al., 1994) (Holtz & Zhao, 2004) (Erwin et al., 2005) (Norris et al., 2008) (Ossicini et al., 2006). Unfortunately, the main difficult in existing doping techniques arises from the fluctuation of impurity number per nanocrystal in a nanocrystal assembly. For Si nanocrystals as small as few nanometers in diameter, the expression of the doping level in the form of "impurity concentration" is not suitable and it should be expressed as "impurity numbers" because it changes digitally. For example, doping of one impurity atom into a nanocrystal of 3 nm in diameter (~ about 700 atoms) corresponds to an impurity concentration of 7.0×10^{19} atoms/cm^3. At this doping level, bulk Si is a degenerate semiconductor and exhibits metallic behavior. However, by means of electron spin resonance (ESR) spectroscopy it was shown that Si nanocrystals do not become metallic even under heavily doped conditions. Therefore, in nanocrystals, addition or subtraction of a single impurity atom drastically changes the electronic structure

and the resultant optical and electrical transport properties. So, for solar cell application, the development of a technique permitting to control the "impurity number" with extremely high accuracy is indispensable.

Up to now, an accurate control of "impurity number" in a Si nanocrystal has not been achieved. One of the largest problems of the growth of doped Si nanocrystals is that impurity atoms are pushed out of nanocrystals to surrounding matrices by the so-called self-purification effect. This effect can be understood by considering very high formation energy of doped nanocrystals (Ossicini et al., 2005). Impurity concentration in nanocrystals is thus always different from average concentration in a whole system. In the worst case, the number of impurity in a nanocrystal becomes zero even when average concentration is rather high. The development of viable technique to characterize impurities, especially "active" impurities doped into nanocrystals, is crucial. The resistivity measurements are thus complemented with ESR spectroscopy as well as PL spectroscopy.

As it was discussed previously, numerous methods have been reported for the growth of intrinsic Si QDs. On the other hand, a limited number of studies are published concerning the growth of shallow impurity-doped Si QDs with the diameter below 10 nm. One of the mostly used methods for shallow-impurity doping of Si nanocrystals is plasma decomposition of SiH_4 by adding dopant precursors (diborane (B_2H_6) and phosphine (PH_3)) (Pi et al., 2008) (Stegner et al., 2008). This method permits to obtain a variety of morphologies from densely packed nanocrystalline films to nanoparticle powder by controlling process parameters (Nychyporuk et al., 2009). Another method is incorporation of doping atoms into SRO layers by simultaneous co-sputtering of Si, SiO_2 and P_2O_5 (or B_2O_3) in SiO_2/SRO superlattice approach described previously (Mimura et al., 2000). During the annealing, Si nanocrystals are grown in phosphosilicate (PSG) (n-type Si QDs) or borosilicate (BSG) (p-type Si QDs) thin films. It should be also noted that the impurity concentration in nanocrystals is different from that of the matrices because the segregation coefficient strongly depends on the kind of impurities and surrounding medium.

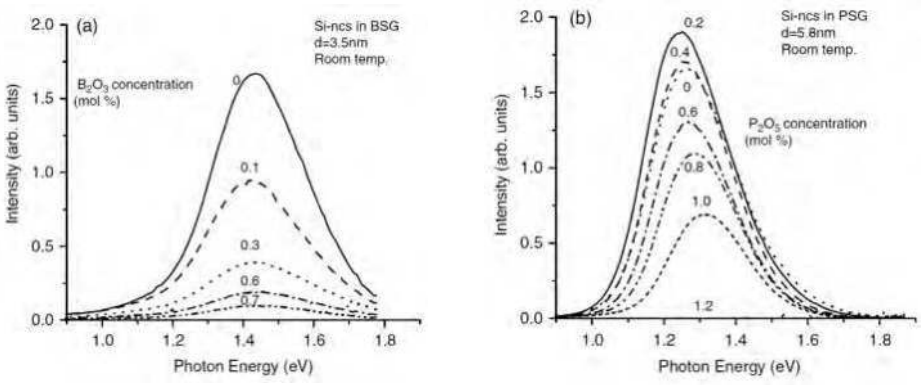

Fig. 9. PL spectra of (a) B-doped (Mimura et al., 1999) and (b) P-doped Si nanocrystals (Fujii et al., 2002) at room temperature for different doping concentrations.

The presence of impurity atoms inside Si nanocrystals can be confirmed by the PL spectroscopy. Indeed, the introduction of extra carriers by impurity doping makes the three-body Auger process possible (Kovalev et al., 2008). In Auger recombination, the energy of

an electron-hole pair is not released in the form of photon. This energy is given to a third carrier, which after the interaction losses its excess energy as thermal vibrations. Since this process is a three-particle interaction, it is normally only significant in strongly non-equilibrium conditions or when the carrier density is very high. For doped nanocrystals the value of Auger rate is four to five orders of magnitude larger than the radiative rate of excitons, and thus one shallow impurity can almost completely kill PL from the nanocrystal. Hence with increasing of average impurity numbers in a nanocrystal assembly, the PL intensity is expected to decrease. This effect was really observed in p-type Si nanocrystals. As one can see on Fig. 9 (a) with increasing of B concentration, the PL intensity monotonously decreases (Fujii et al., 1998) (Müller et al., 1999) (Stegner et al., 2008).
In P-doped Si nanocrystals, the situation is different. When the phosphorous concentration is relatively low, the PL intensity increases slightly compared to that of the undoped Si nanocrystals (Fig. 9 b) (Fujii et al., 2000) (Mimura et al., 2000) (Tchebotareva et al., 2005). The increase of the PL intensity indicates that non-radiative recombination processes are quenched by P doping. One of the possible explanation is that electrons supplied by P are captured by the dangling bonds, which inactivate the nonradiative recombination centers and compensate donors (Stegner et al., 2008) (Lenahan et al., 1998). It should be also noted that the PL intensity also strongly depends on the size of the shallow-doped Si nanocrystals.
There are many theoretical studies on preferential localization of impurities in Si nanocrystals. It should to be noted that it is almost impossible to control experimentally the location of impurities in nanocrystals. However, the information on localization was experimentally obtained (Kovalev et al., 1998). It was shown that P dopants are localized at or close to the surface of Si nanocrystal. On the contrary, the B atoms are primary incorporated into the Si nanocrystal core. However, the preferential localization of impurities may depend on nanocrystal growth process and the surface termination. Therefore, properties of dopant may be quite different between Si nanocrystals grown by the decomposition of SiH_4, phase separation of SRO and so on. In any cases the doping efficiency by B atoms is much smaller than that of P atoms due to larger formation energy of B-doped Si nanocrystals than P-doped ones (Kovalev et al., 1998) (Ossicini et al., 2005).
To what concerns the optical and electrical properties, contrary to the intrinsic Si nanocrystals, the shallow doped Si nanocrystals present new degree of freedom to control them. For example, the size is one of the main parameters to control optical bandgap of the intrinsic Si nanocrystals. On the other hand, due to the difference in the electronic band structure in the case of doped and codoped Si nanocrystals (obtained by the simultaneous doping by B and P atoms), the optical bandgap is determined by the combination of the size and impurity concentration (Fujii et al., 2010).
It is worth noting that the impurity atoms alter the formation kinetics of Si nanocrystals. Indeed, the average size of P-doped Si nanocrystals is increased compared to the undoped ones under the same experimental conditions (Conibeer et al., 2010), and in some experiments this increasing was almost double. Contrary to the doping with P, the doping with B results in the forming of smaller Si nanocrystals compared to the undoped case (Hao et al., 2009). The crystalline volume fraction was found to decrease with increasing of B concentration (Hao et al., 2009), which suggests that boron suppresses Si crystallization. One of the possible reasons is the local deformations induced by the impurity atoms.

3.2.1 Dark resistivity measurements

The resistivity of the Si QD material is an important parameter for photovoltaic applications. The influence of the doping concentration on resistivity of Si QD superlattices was studied

(Hao et al., 2009, 2009a), (Conibeer et al., 2010) (Ficcadenti et al., 2009). The contact resistances in the above measurements were determined by using the TLM (Transmission Line Model) method proposed by Reeves and Harrison (Reeves & Harrison, 1982). This method involves measurement of the resistance between several pairs of contacts, which have identical areas, but are separated by different spaces (Fig. 10). The dark resistivity is then defined as: $\rho_{dark} = V \times d \times w / I \times l$, where d is the thickness of Si QD superlattice, w is the length of Al pad and l is the spacing of Al pads.

To perform the dark resistivity measurements, the Si QD superlattices were grown on the quartz substrate. The ohmic contacts were obtained by thermal evaporation of Al, followed by sintering at a temperature (500-530°C) lower than the Al-Si eutectic temperature to allow the Al to spike down into the film (Voz et al., 2000). The schematic view of the final structure for the lateral resistivity measurements is presented on the Fig. 10.

Fig. 11 (a) and (c) represents the room temperature dark resistivity of Si QD/SiO_2 multilayer films for various phosphorous and boron doping levels, respectively. As one can see, the introduction of a slight amount of P and B drastically changes the dark resistivity of the films, from 10^8 Ωcm for the undoped samples to 10^2 – 10 Ωcm for doped ones, which is 6 -7 orders of magnitude lower than that of the undoped samples. This decrease in resistivity may be the consequence of an increase in mobile carrier concentration due to a rise in the number of active dopants in the film.

The TLM method was also used to measure the temperature dependence of the resistance of the Si QD films with various (b) phosphorous (Hao et al., 2009) and (d) boron (Hao et al., 2009) concentrations (Fig. 11 (b) and (d), respectively). These measurements permit to estimate the values of the activation energy (E_a), that is in a n- (p-) doped semiconductor the energy difference between the conduction (valance) band and Fermi level. The activation energy was calculated by using relation $R \approx exp(E_a/kT)$. As one can see, with the increasing of the doping level, for both types of impurities the activation energy decreases from ~0.5 eV to 0.1 eV. This result is consistent with the view that the observed resistivity decreases are a consequence of an increase in carrier concentration due to more active dopants in the film. The decrease in E_a accompanying the drop in resistivity indicates that the Fermi level energy is moving toward the conduction (valance) band for n- (p-) type doped Si QDs.

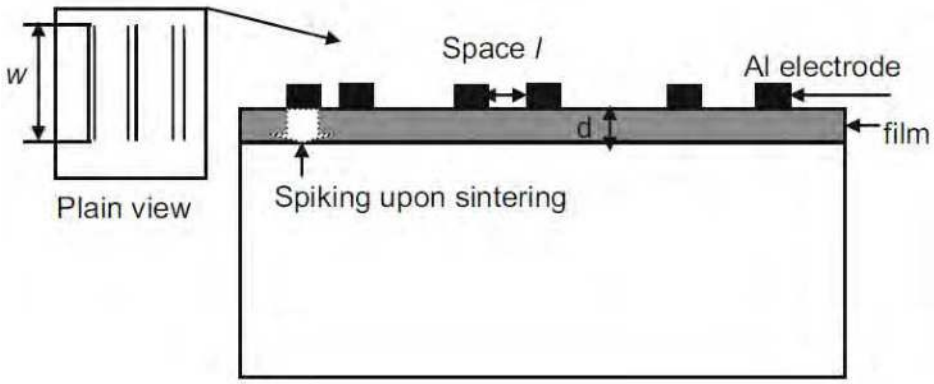

Fig. 10. Schematic layout of the Al contacts on a film for dark resistivity measurements (Hao et al., 2009).

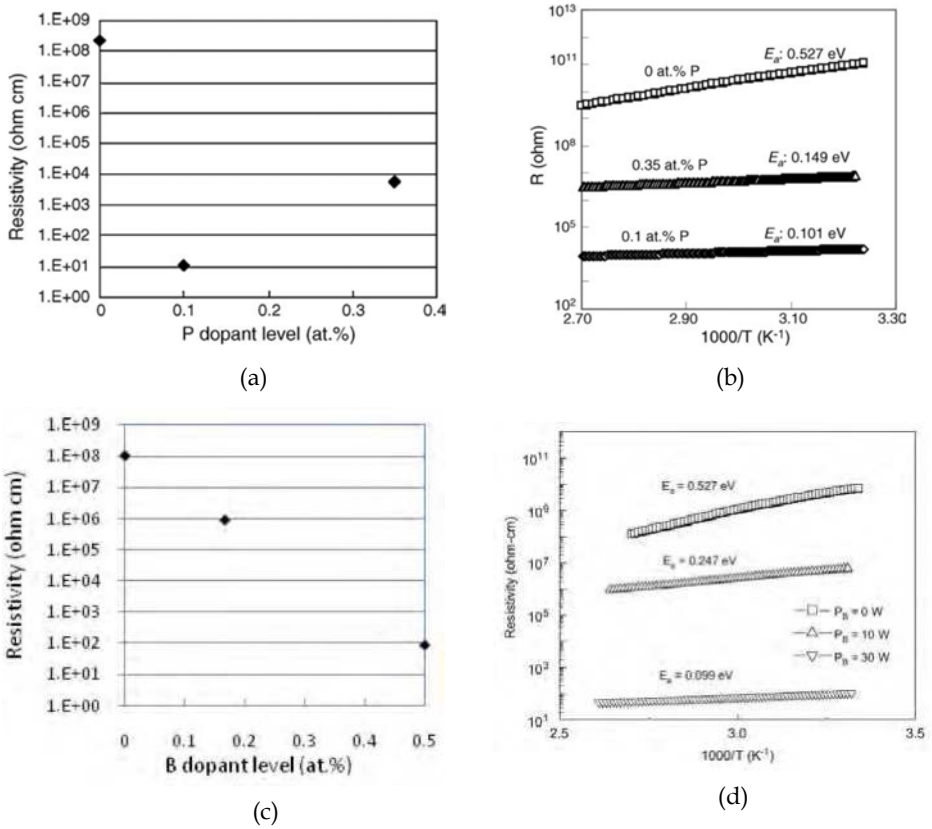

Fig. 11. Dark resistivity of Si QD/SiO_2 multilayer films for various (a) phosphorous (Hao et al., 2009) and (c) boron (Conibeer et al., 2010) doping levels.; Temperature dependence of the resistance of the Si QD films with various (b) phosphorous (Hao et al., 2009) and (d) boron (Hao et al., 2009) concentrations .

3.3 Optical properties of Si QDs

Regarding to photovoltaic applications, the optical bandgap and the absorption coefficient of Si QDs are the very first physical parameters to be studied and optimized prior to solar cell fabrication. Optical methods provide an easy and sensitive tool for measuring the electronic structure of quantum objects, since they require minimal sample preparation and the measurements are sensitive to the quantum effects. The energy gaps of Si QDs could be determined, for example, from photoluminescence (PL) measurements, whereas the absorption coefficient from the transmission-reflection measurements.

3.3.1 Bandgap of Si QDs

Experimental energy gaps of isolated Si QDs in SiO_2 and SiN_x matrices reported by several research groups are shown on Fig. 12 (Cho et al., 2004) (Park et al., 2000) (Takeoka

et al., 2000). As one can see the bandgap values of Si nanostructured material could be adjusted in the large range (up to 3.1 eV), covering an important part of the solar spectrum. The results obtained by different teams are in good agreement where the matrix is the same but are quite different for QDs in oxide compared to nitride, particularly for small QDs. They are also qualitatively consistent with the results from *ab-initio* modeling (König et al., 2009) (Ögüt et al., 1997), which had been carried out for the confined energy levels in Si QD consisting of a few hundred atoms. One can observe the expected increasing of confinement energy with decreasing QD size, but also that the amino-terminated QDs (silicon nitride) have energies about 0.5 eV more than the hydroxyl-terminated ones (silicon oxide). The last one observation is consistent with the explanation for the enhanced energies of QDs in nitride given by Yang et al (Yang et al., 2004), that the reason for it is due to better passivation of Si QDs by nitrogen atoms eliminating the strain at the Si/Si_3N_4 interface.

Influence of interconnections between the QDs on tuning of their bandgap was also studied (Nychyporuk et al., 2009) (Degoli et al., 2000). Indeed, electronic coupling between the neighboring low-dimensional Si nano-objects constituting a complex quantum system must be considered. This coupling leading to intense energy transfer processes between the electronically communicating quantum objects determines physical properties of the whole quantum system and, therefore, has to be taken into account, of course. It was shown that when the nanocrystals (Allan & Delerue, 2007) (Bulutay, 2007) start to touch each other, the bandgap value of the assembly begins to decrease rapidly (Fig. 13). Thus, the bandgap of the interconnected nanostructures depends not only on the nanocrystal dimension but also on the degree and number of interconnections between them.

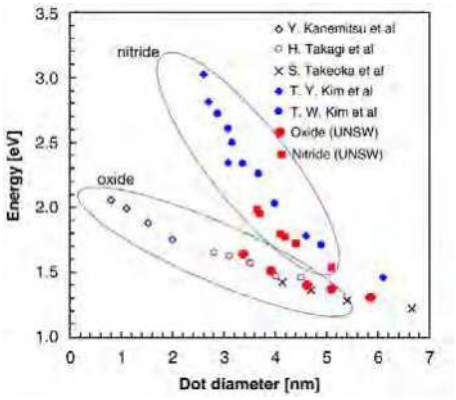

Fig. 12. Experimental energy gaps of three-dimensionally confined Si QDs in SiO_2 and SiN_x matrices (300°C) for several research groups (Takeoka et al., 2000) (Kim et al., 2004), (Kim et al., 2005) (Yang et al., 2004) (Fangsuwannarak, 2007).

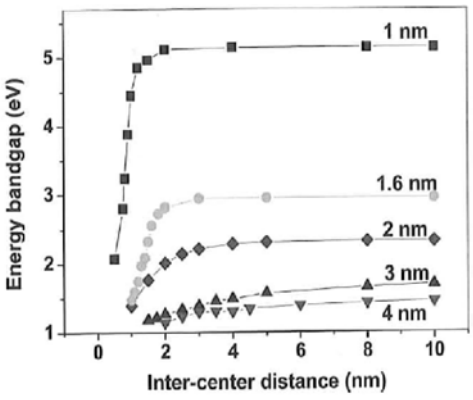

Fig. 13. Evolution of the bandgap of the quantum system constituted of 27 interconnected Si QDs as a function of the distance between the QDs.

3.3.2 Optical absorption of Si QDs

The absorption coefficient was experimentally determined for Si QDs in deferent matrices. Fig. 14 shows the global absorption coefficient of SiN_x layers of different stoichiometries with Si QDs embedded inside (Nychyporuk et al., 2008). The absorption coefficient of polycrystalline silicon (poly-Si) is also added for comparison. As it can be seen, the global absorption coefficient of the composite SiN_x decreases with stoichiometric ratio R (i.e. with decreasing of Si QD size and density) and its band-edge shifts to higher energies. Its magnitude is being much lower than that one of the absorption coefficient of poly-Si. No evidence of oscillator strength enhancement was observed and the global absorption coefficient is limited principally by the volume fraction of Si QDs inside the dielectric matrices. These why, the maximum absorption coefficient, approaching this one of the bulk Si, was found in the case of interconnected Si QDs forming thin films (Nychyporuk et al., 2009).

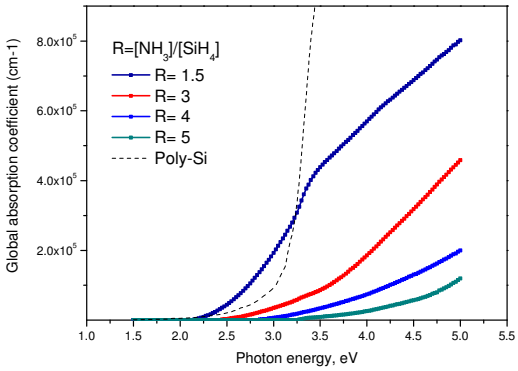

Fig. 14. Global absorption coefficient of SiN_x layers of different stoichiometries with embedded Si QDs. The absorption coefficient of poly-Si is also presented for comparison (Nychyporuk et al., 2008).

3.4 Electrical transport mechanisms in Si QD ensembles

While the optical properties of the various ensembles of individual Si nanocrystals have been investigated by many researchers, relatively little attention was paid to the transport properties of 3D ensembles of such QDs. In this paragraph we will only briefly review the main results on the transport mechanisms obtained previously in the literature. A complete review of the electrical transport mechanisms in 3D ensembles of disordered Si nanocrystallites embedded in insulating continuous matrices can be found in Ref. (Balberg et al., 2010). To what concerns the transport processes in nanocrystalline Si superlattices, they were well reviewed in Ref. (Lockwood & Tsybeskov, 2004).

3.4.1 Disordered Si QDs in insulating matrix

The transport properties of the ensembles of disordered Si QDs in insulating matrix could be explained in terms of the percolation theory, which has already been successfully implemented to explain the transport processes in granular metals (Abeles et al., 1975).

Indeed, this theory describes the effect of the system's connectivity on its geometrical and physical properties. In the case of granular metals, in a system of N metallic spheres embedded randomly in an insulating matrix, there will be a critical density of spheres N_c above which a "continuous" metallic network will be formed and a metallic bulk-like conduction will dominate. Correspondingly, N_c is the classical percolation threshold (Fonseca & Balberg, 1993) (Balberg et al., 2004). For $N < N_c$, the electron transfer between the individual grains is possible only by tunneling (Abeles et al., 1975) (Balberg et al., 2004).

To what concerns the ensemble of Si QDs, there can be distinguished five different structural-electrical regimes, such that in each of them we may expect a different transport mechanism to dominate. These regimes are *(a)* uniformly dispersed in insulating matrix isolated spherical QDs; *(b)* the transition regime, where some of the QDs starts to "touch" their neighbors; *(c)* the intermediate regime, where clusters of "touching" QDs are formed; *(d)* the percolation transition regime where the above clusters form a global continuous network; and *(e)* the regime where the percolation cluster of "touching" QDs is well formed and geometrically non-"touching" QDs are rarely found. Fig. 15 (a), (b) and (c) present typical examples of ensembles of Si QDs corresponding to regimes *(a)*, *(c)* and *(e)*, respectively. It is worth noting that the connectivity between "touching" QDs in ensembles of semiconductor QDs is different than in granular metals. Usually there are narrow (no more than 0.5 nm wide) boundaries formed between the nanoparticles, which involves at least a different crystallographic orientation of the touching crystallites. This quantum size "grain boundary" limit has not been studied so far. In a literature the charge transfer process between such "touching" QDs was termed as "migration" (Antonova et al., 2008) (Balberg et al., 2007).

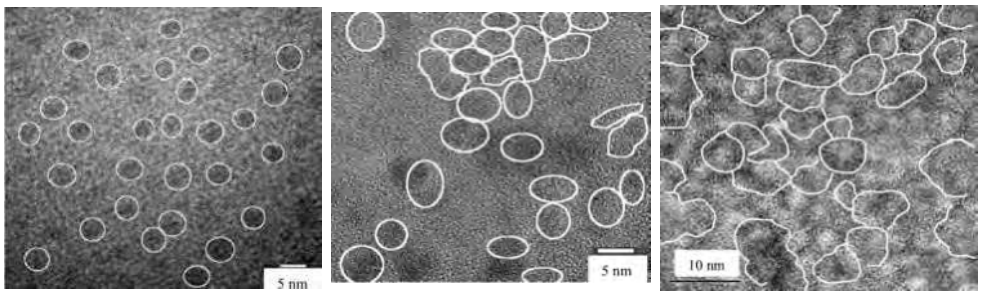

(a) (b) (c)

Fig. 15. HRTEM images of the ensembles of Si QDs corresponding to different structural-electrical regimes: (a) uniformly dispersed isolated spherical QDs (regime *a*), (b) clusters of "touching" QDs (regime *c*) and (c) percolation clusters of "touching" QDs (regime e) (Antonova et al., 2008).

The effect of the connectivity on the transport properties (dark and photoconductivity) of the ensembles of Si QDs is illustrated on Fig. 16. As one can see, the global picture of transport in Si QDs ensembles is reminiscent of that of granular metals, but the details are quite different. For the samples with low Si content (related to the number of Si QDs in the ensemble), which are characterized by the isolated Si QDs (regime *a*), the local conductivity

is determined by the tunneling of charge carriers under Coulomb blockage[2] between adjacent nanocrystallites similar to the case encountered in granular metals in the dielectric regime (Abeles et al., 1975) (Balberg et al., 2004). Indeed, as long as Si QDs or clusters of Si QDs are small enough, they "keep" the carrier that resides in them and become charged when an excess charge carrier reaches them. Hence, the transport through the system can take place only if a corresponding charging (or Coulomb) energy is provided.

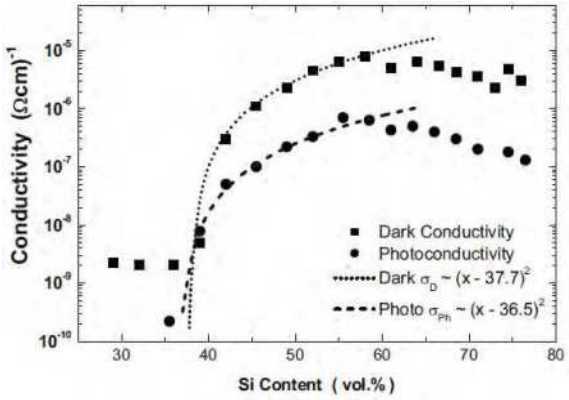

Fig. 16. Dependence of the dark conductivity and the photoconductivity on the Si content (related to the number of Si QDs in ensemble)

With increasing of Si content (Fig. 15 (b)), the interparticle distance decreases and the tunneling-connected quantum dot clusters grow in size. The "delocalization" of the carrier from its confinement in the individual quantum dot to larger regions of the ensemble will take place, i.e., the charge carrier will belong to a cluster of QDs rather than to an individual QD. Correspondingly, this will also yield a decrease in the local charging energy in comparison with that of the isolated QD and the distance to which the charge carrier could wander will increase and as a consequence the conductivity of the ensemble will increase as well. The charge carrier transport in the case of regime *(c)* is thus determined by the intracluster migration and by the intercluster tunneling.

As one can see from the Fig. 16, the maximal possible conductivity is assured in the case of highly percolating system of Si QDs (regime *(e)*). However, the conduction in this regime is quite different from that one of the granular metals since there are still boundaries between touching Si QDs. In fact, the corresponding migration process is similar to that in polycrystalline semiconductors, but now the boundaries are on the quantum scale. It was suggested that in this regime the migration dominates the transport properties and the global conductivity is limited by the interface between the touching QDs (Balberg, 2010).

[2] The transfer of an electron from a given neutral particle to an adjacent neutral particle, charges this particle by one (positive) elementary charge *(q)* and that of the adjacent particle by one (negative) elementary charge. If the capacitance of the individual particle in its corresponding environment is C_0, the energy needed to be supplied for the above "electron-hole" transfer by tunneling is then: $E=q^2/C_0$. This energy, which opposes to the transfer of charge carriers, is known as the Coulomb blockage energy, which is of the order of a tenth of an eV. In general, one can say, that a tunneling process is thermally activated when it requires a supply of energy.

Form the photovoltaic point of view, the thin films constituted of interconnected Si QDs are the most promising candidates for higher bandgap materials in all-Si tandem cell approach. Indeed, the highly percolating system of Si QDs will ensure the most favorable conditions for the electronic transport between the nanocrystals and, as it was discussed previously, the bandgap value in such structures could be adjusted in the large range covering the major part of the solar spectrum (Nychyporuk et al., 2009).

3.4.2 Nanocrystalline Si superlattices

Nanocrystalline Si superlattices have been proposed as candidates for the high bandgap absorber component in all-Si tandem solar cells. They consists of thin dielectric and Si QD based layers alternating in one direction, i.e., heterostructure type –I superlattices. The period of such a superlattice usually is much larger than the lattice constant but is smaller than the electron mean free path. Such a structure possesses, in addition to a periodic potential of the crystalline lattice, a potential due to the alternating semiconductor layers. The existence of such a potential significantly changes the energy bandstructure of the semiconductors from which the superlattice is formed. The coupling among QDs occurs, leading to a splitting of the quantized carrier energy levels of single dots and formation of three-dimensional minibands (Lazarenkova & Balandin, 2001) (Jiang & Green, 2006) as sketched on Fig. 17 (shaded areas).

The charge carrier mobility, which has a crucial impact on a charge-collection efficiency in solar cells, depends on the dominant transport regime at given operating conditions, which may be described by mini-band transport, sequential tunneling or Wannier-Stark hopping (Wacker, 2002). The sequential resonant tunneling (SRT) was suggested to be the most prominent for efficient carrier collection in Si QD solar cells (Raisky et al., 1999).

The schematic view of the sequential resonant tunneling transfer in a multiple-quantum-well structure is depicted on Fig. 18. Electrons tunnel from the ground state of the j^{th} well into an excited state of the $(j+1)^{th}$ well. The tunneling process is then followed by intrasubband energy relaxation from the excited state to the ground state. This two-step scheme can be repeated as many times as needed to build the required thickness for optimal solar absorption. Resonance occurs when the E_2-$E_1 = |q\mathbf{F}d|$ condition is satisfied where E_1 and E_2 are the ground and first excited subband energies of the quantum well, q the electron charge, $\boldsymbol{F}$ the internal electric field, and d the spatial structural period. From Fig. 18 it is clear that the bottleneck of electron transfer is the last (N^{th}) well, where carriers have to transfer through a significantly thicker right barrier than inside the multiple-quantum-well region. This can lead to charge build up and, consequently, screening of the built-in field.

The photogeneration and transport in superlattice absorbers, on the example of a Si-SiO_x multilayer structure embedded in the intrinsic region of a p-i-n diode was recently numerically investigated (Aeberhard, 2011). The model system under investigation is shown on the Fig. 19. It consists of a set of four coupled quantum wells of 6 monolayer[3] (ML) width with layers separated by oxide barriers of 3-ML thickness, embedded in the intrinsic region of a Si p-i-n diode. The doping density was 10^{18} cm^{-3} for both electrons and holes. Insertion of the oxide barriers leads to an increase of the effective bandgap in the central region of the diode from 1.1 to 1.3 eV. The spectral rate of carrier generation in the confined states under illumination with monochromatic light at photon energy 1.65 eV and intensity of 10 kW/m^2

[3] The monolayer thickness is half the Si lattice constant, i.e., 2.716 Å.

is shown on the Fig. 20. At this photon energy both the lowest and the second minibands are populated. The photocurrent originating in this excitation is shown on Fig. 21. Current flows also in first and second minibands, which means that relaxation due to scattering is not fast enough to confine transport to the band edge. However, transport of photocarriers is strongly affected by the inelastic interactions, and is the closest to the sequential tunneling regime. We can thus conclude that in the case of high internal fields, excess charge is transported via sequential tunneling in the miniband where it is generated.

The sequential resonance tunneling enhances the photocarrier collection and reduces radiative recombination losses (Raisky et al., 1999). However it should be noted that SRT increases both photocurrent (Iph) and dark current (Idc). The total current of a photovoltaic device is the difference of these two currents, and thus, to take advantage of SRT, a solar cell possessing a superlattice structure should be designed to have the resonance in the region where $I_{ph} \gg I_{dc.}$

The main challenge of the tandem structure is to achieve sufficient carrier mobility and hence a reasonable conductivity. This generally requires formation of a true superlattice with overlap of the wave function for adjacent QDs, which in turns requires either close spacing between Si nanocrystals or low barrier height. Transport properties strongly depend on the matrix in which the Si quantum dots are embedded. Indeed, the electron or the hole wavefunctions exponentially decay with distance. Fig. 22 shows the penetration length of the wave function of electron of a single quantum well into different high-bandgap materials having different barrier heights. As one can see, the tunneling probability heavily depends on the barrier height. The penetration length is bigger for the materials with lower barrier height. Thus Si_3N_4 and SiC giving lower barriers than SiO_2, allow larger dot spacing for a given tunneling current. For example, the QDs in SiO_2 matrix would have to be separated by no more than 1-2 nm of matrix, while they could be separated by more than 4 nm of SiC.

The influence of the fluctuations in spacing and size of the QDs on the carrier mobility was also investigated (Jiang & Green, 2006). The calculations have shown that the interdot distance has larger impact on the calculated carrier mobility while the dot size can be used to control the band energy level.

3.5 Fabrication of Si QD PV devices

Recently it have been reported on the realization of interdigitated silicon QD solar cells on quartz substrate(Conibeer et al., 2010). Schematic view of the fabricated solar cells is shown on the Fig. 23 (a). The p-n diodes were fabricated by sputtering alternating layers of SiO_2 and SRO onto quartz substrate with in situ B and P doping. The top B doped bi-layers were selectively etched to create isolated p-type mesas and to access the buried P doped bi-layers. Aluminium contacts were deposited by evaporation, patterned and sintered to create ohmic contacts on both p- and n-type layers. The area of the fabricated interdigitated solar cells was 0.12 cm^{-2}. One of the derivatives of the presented approach was the fabrication of the p-i-n diodes. Indeed, it is expected that the intrinsic layer will have a longer lifetime that the doped material leading to an improved photocurrent.

I-V measurements in the dark and under 1-sun illumination (Fig. 23 (b)) indicate a good rectifying junction and generation of an open-circuit voltage, V_{OC}, up to 492 mV (Conibeer, 2010). The high sheet resistance of the deposited layers, in conjunction with the insulating quartz substrates, causes an unavoidable high series resistance in the device.

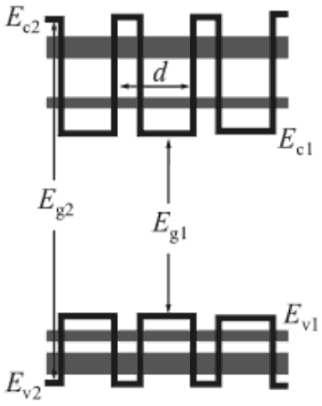

Fig. 17. The energy bandstructure of a semiconductor type-I heterostructure superlattice : E_{g1} and E_{g2} are the bandgaps, E_{c1} and E_{c2} are the bottoms of the conduction bands of narrow bandgap and wide bandgap semiconductors, respectively; d is the period of the heterostructure superlattice (Mitin, 2010).

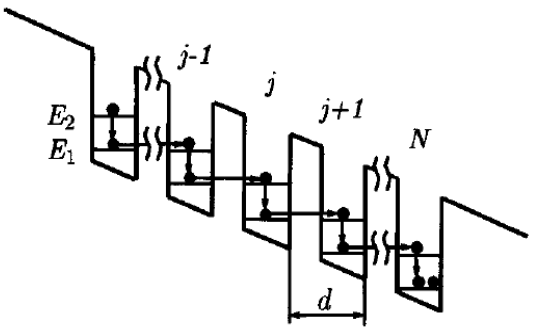

Fig. 18. Sequential resonant tunneling transfer in multiple-quantum-well structure. E_1 and E_2 are the energies of the ground and first excited states in the quantum well, respectively, and d the superlattice period (Raisky et al., 1999).

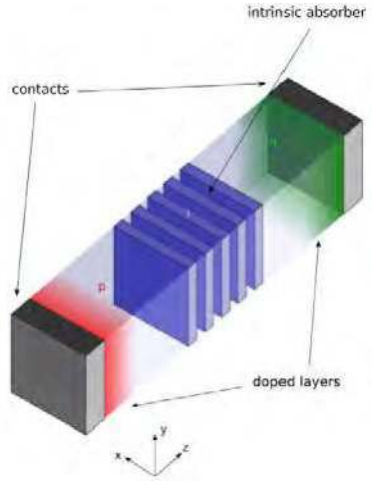

Fig. 19. Spatial structure and doping profile of the p-i-n model system (Aeberhard, 2011).

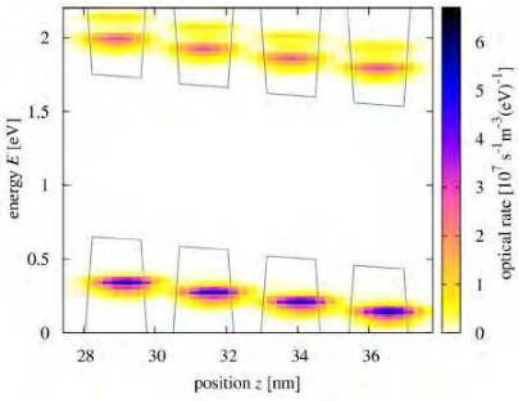

Fig. 20. Spatially and energy resolved charge carrier photogeneration rate in the quantum well region at short-circuit conditions and under monochromatic illumination with energy of 1.65 eV and intensity of 10kW/m^2 (Aeberhard, 2011).

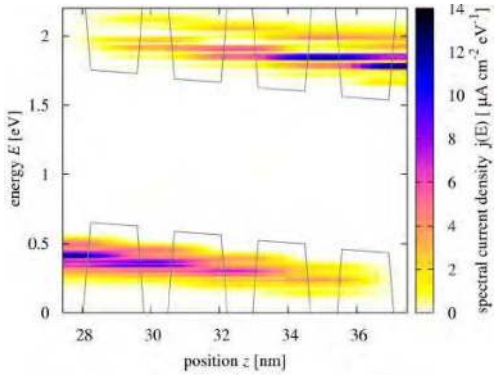

Fig. 21. Spatially and energy-resolved charge carrier short-circuit photocurrent density in the quantum well region under monochromatic illumination with energy of 1.65 eV and intensity of 10kW/m² (Aeberhard, 2011).

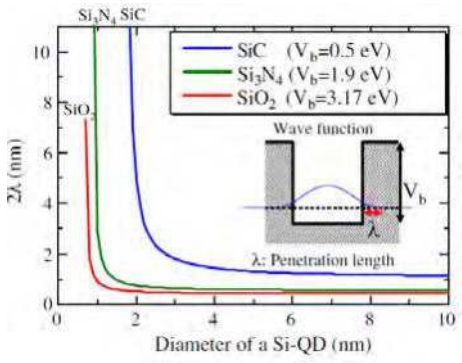

Fig. 22. Penetration length of the wave function of confined electron into barrier layers. V_b represents a barrier height for each barrier material (Aeberhard, 2011).

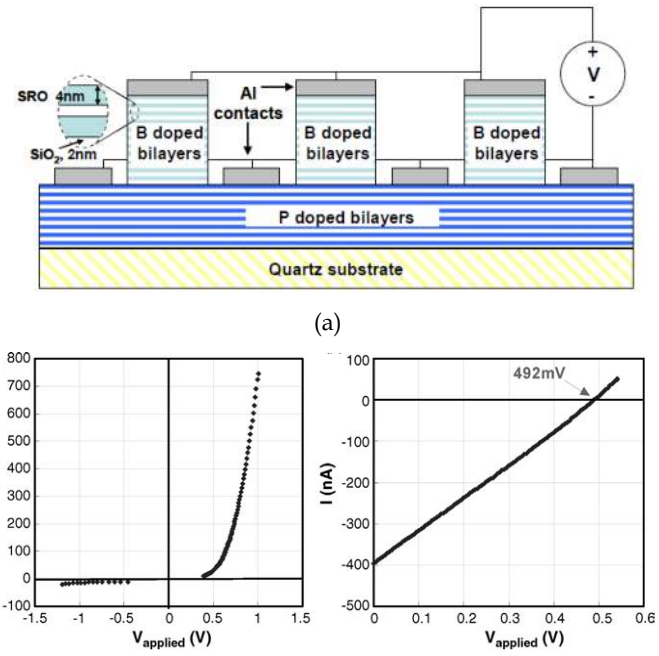

Fig. 23. (a) Schematic representation of the fabricated interdigitated devices (Conibeer et al., 2010); (b) Dark and illuminated I-V measurements of p-i-n diodes with 4 nm SRO/2 nm SiO2 bilayers.

The high resistance severely limits both the short-circuit current and the fill factor of the cells, particularly under illumination. Significant improvement is expected once the parasitic series resistance is eliminated.

Further evidence that this photovoltaic effect occurs in a material with an increased bandgap is given by temperature dependent I-V mesurements, from which an electronic bandgap for the Si QD nanostructure materials can be extracted. A bandgap of 1.8 eV was extracted for a structure containing Si QDs with a nominal diameter of 4 nm. However, this value will be due to a combination of other components in series with the material bandgap, hence the true material bandgap will be less than 1.8 eV.

Homojunction Si QD devices have also been fabricated in a SiC matrix using the superlattice approach (Song et al., 2009). Fig. 24 (a) shows a schematic diagram of a n-type Si QD: SiC/ p-type Si QD:SiC homojunction solar cell fabricated on a quartz substrate. The n-type Si QD emitter was approximately 200 nm thick and the p-type base layer is approximately 300 nm thick. This devices have given V_{OC} of 82 mV that is promising initial value for a Si QDs in SiC solar cells on quartz substrate. Improvement of the device structure and optimization of dopant incorporation is expected to improve this value.

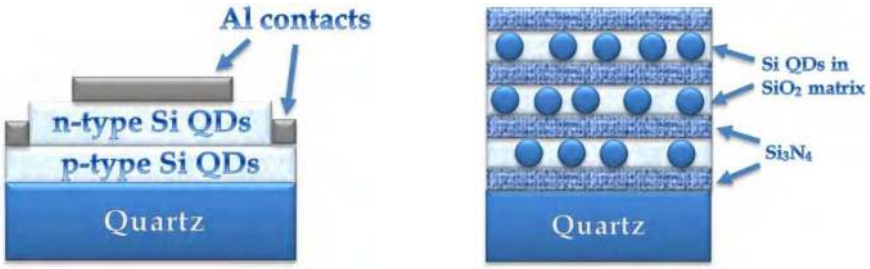

(a) (b)

Fig. 24. (a) Schematic diagram of a n-type Si QD: SiC/ p-type Si QD:SiC/ quartz homojunction solar cell (Song et al., 2009); (b) The concept of the transport improvement: alternating layers of Si_3N_4 and SRO.

Current in both these SiO_2 and SiC matrix devices was very small, due principally to the very high lateral resistance and also because of the small amount of absorption in the approximately 200 nm of material used. Indeed, as it was discussed in the previous paragraph, transport in these devices relies on tunneling and hopping between adjacent QDs. To maximize the tunneling probability, the barrier heights between QDs must be low, but this then compromises the degree of quantum confinement and the height of the confined energy levels and hence the effective bandgap obtained. The solution is to introduce anisotropy between the growth, *z*, direction and the *x*-*y* plane. This can achieved by maintaining strong confinement through the use of a large barrier height oxide in the plane, but to intersperse these layers with layers of lower barrier height such as Si_3N_4 or SiC, thus giving higher tunneling probability in the z direction (Fig. 24 (b)) (Di et al., 2010). The very first results on this approach were rather promising and showed the decreasing in the vertical resistivity of such Si QD nanostructures with SiN_x interlayers (Di et al., 2010). To what concerns the increasing of the V_{OC} the most potential route is the passivation of the defects through the hydrogenation.

The first prototypes of Si QD PV devices were successfully developed. Up today they present V_{OC}, I_{SC} and fill factor (FF) values which still lower than those ones of the 1st generation PV cells based on bulk Si – but all these problems are being addressed. The next step implies the further optimization of the fabrication parameters, developing of the efficient doping technique and defect passivation.

4. Silicon nanowire solar cells

Nanowire solar cells demonstrated to date have been primarily based on hybrid organic-inorganic materials or have utilized compound semiconductors such as CdSe. Huynh *et al*. utilized CdSe nanorods as the electron-conducting layer of a hole conducting polymer-matrix solar cell (Huynh et al., 2002) and produced an efficiency of 1.7 % for AM 1.5 irradiation. Similar structures have been demonstrated for dye-sensitized solar cells using titania or ZnO nanowires, with efficiencies ranging from 0.5 % to 1.5 % (Law et al., 2005). These results show the benefits of using nanowires for enhanced charge transport in nanostructured solar cells compared to other nanostructured architectures. The Si nanowires (Si NW) solar cells have a potential to provide the equal or better performance to crystalline Si solar cells with processing methods similar to thin film solar cells (Tsakalakos et al., 2007) (Uchiyama et al., 2010) (Andra et al., 2008).

4.1 Fabrication of Si nanowires

The techniques to produce nanowires are normally divided into *(i)* bottom up and *(ii)* top down approaches.

4.1.1 Bottom up approach

The bottom up approach starts with individual atoms and molecules and builds up the desired nanostructures. One of the mostly used methods in this family of approaches is the Vapor Liquid Solid (VLS) method which uses metal nanotemplates on Si wafer or on Si thin film (Kelzenberg et al., 2008) (Tian et al., 2007) (Tsakalakos et al., 2007, 2007a). In this method a liquid metal cluster acts as the energetically favored site for vapor-phase reactant absorption and when supersaturated, the nucleation site for crystallization. An important feature of this approach for nanowire growth is that phase diagrams can be used to choose a catalyst material that forms a liquid alloy with the nanowire material of interest, i.e. Si in our case. Also, a range of potential growth temperatures can be defined from the phase diagram such that there is coexistence of liquid alloy with solid nanowire phase. The main advantages of the VLS method which should be cited are the rather high growth rate of several 100 nm/min and the fact that perfectly single crystalline nanowires form.

A schematic diagram illustrating the growth of Si nanowires by the VLS mechanism is shown on (Fig. 25 (a)). When the nanocatalysts become supersaturated with Si, a nucleation event occurs producing a solid/liquid Si/Au-Si alloy interface. In order to minimize the interfacial free energy, subsequent solid growth/crystallization occurs at this initial interface, which thus imposes the highly anisotropic growth constrain required for producing nanowires. Its growth continues in the presence of reactant as long as catalyst nanocatalyst remains in the liquid state. Typically the growth is performed by using SiH_4 as the Si reactant, and diborane and phosphine as p- and n-type dopants, respectively. The growth can be carried out using Ar, He or H_2 as carrier gas, which enables an added degree of freedom for the nanowire growth. For exemple, the use of H_2 as a carrier gas can

passivate the growing solid surface and reduce the roughness (Wu et al., 2004) while Ar and He can enhance radial deposition of a specific composition shell.

Most frequently gold is taken as a template for nanowire growth. The Au-Si binary phase diagram (Fig. 25 (b)) predicts that Au nanocatalysts will form liquid alloy droplets with Si at temperatures higher than the eutectic point which is 363°C. The Au nanocatalysts can be prepared either from commercially available gold colloids or by depositing a thin Au film followed by a heating step above the eutectic temperature during which a Au-Si liquid film forms to disintegrate into nano-droplets. Another simple and effective method for producing metal nanoparticles (Au, Ag…) at room temperature is based on their electroless deposition on the surface of Si or hydrogenated Si nitride films (Nychyporuk et al., 2010). It should be mentioned that it is still a controversial issue how gold is incorporated into the wire and thus how it influences the electronic properties of the nanowire. Gold is a deep-level defect in bulk Si and if it is also true for nanowires grown from Au droplets. Hence the alternative metals like In, Sn, Al (Ball et al., 2010) are actually under investigation for using as nanocatalysts during the nanowire growth.

Si NWs grow with a diameter similar to that of the template droplet. The nanowire diameters are on average 1-2 nm larger than the starting nanocatalyst size. As a result a carpet of perfect single crystalline NWs of 10 to 200 nm in diameter and several micrometers in length can be grown on the crystalline substrate (Fig. 26 (a)) (Andra 2008). High-resolution transmission electron microscopy (HRTEM) was used to define in detail the structures of these nanowires (Wu et al., 2004). As synthesized Si NWs are single crystalline nanostructures with uniform diameters. Studies of the ends of the nanowires show that they often terminate with Au nanoparticles (Fig. 26 (b)). In addition, the crystallographic growth directions of Si NWs have also been investigated using HRTEM and systematic measurements reveal that the growth axes are related to their diameters (Wu et al., 2004) (Cui et al., 2001a). For diameters between 3 and 10 nm, 95% of the Si NWs were found to grow along the <110> direction, for diameters between 10 and 20 nm, 61% of the Si NWs grow along the <112> direction, and for diameters between 20 and 30 nm, 64% of the Si NWs grow along the <111> direction. These results demonstrate a clear preference for growth along the <110> direction in the smallest Si NWs and along <111> direction in larger ones (Zhong et al., 2007). Cross-sectional HRTEM analysis has revealed that the nanowires could have triangular, rectangular and hexagonal cross section with well – developed facets (Vo et al., 2006) (Jie et al., 2006) (Zhang et al., 2005).

The VLS method permits to fabricate the nanowires of well-defined length with diameters as small as 3 nm (Wu et al., 2004). The electronic properties can be precisely controlled by introducing dopant reactants during the growth. Addition of different ratios of diborane or phosphine to silane reactant during growth produces p- or n- type Si nanowires with effective doping concentrations directly related to the silane: dopant gas ratios (Cui et al., 2000) (Cui et al., 2001) (Zheng et al., 2004) (Fukata, 2009). It was demonstrated that B and P can be used to change the conductivity of Si NWS over many orders of magnitude (Cui et al., 2000). The carrier mobility in SiNWs can reach that one in bulk Si at a doping concentration of 10^{20} cm^{-3} and decreases for smaller diameter wires. Temperature dependent measurements made on heavily doped SiNWs show no evidence for single electron charging at temperatures down to 4.2 K, and thus suggest that SiNWs possess a high degree of structural and doping uniformity. Moreover, TEM studies of boron- and phosphorous doped SiNWs have shown that contrary to Si QDs the introduction of impurity atoms during the nanowire growth does not change their crystallinity. The ability to prepare well-defined doped nanowire during synthesis distinguishes nanowires from QDs.

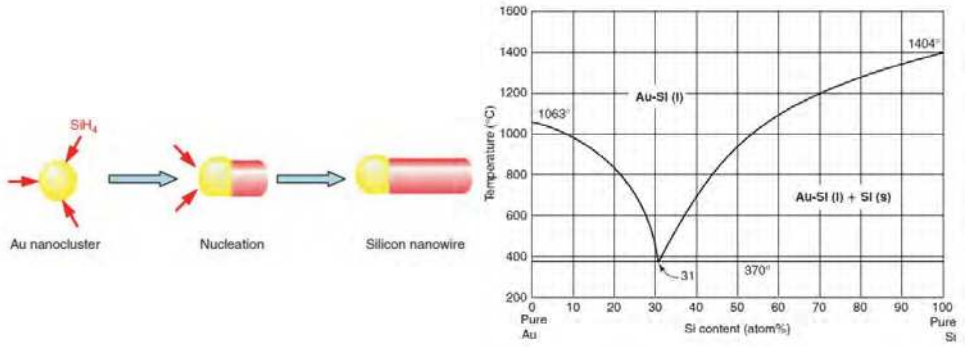

(a) (b)

Fig. 25. (a) Schematic diagram illustrating the growth of Si nanowires by the VLS mechanism. (b) Binary phase diagram of Au-Si (Zhong et al., 2007).

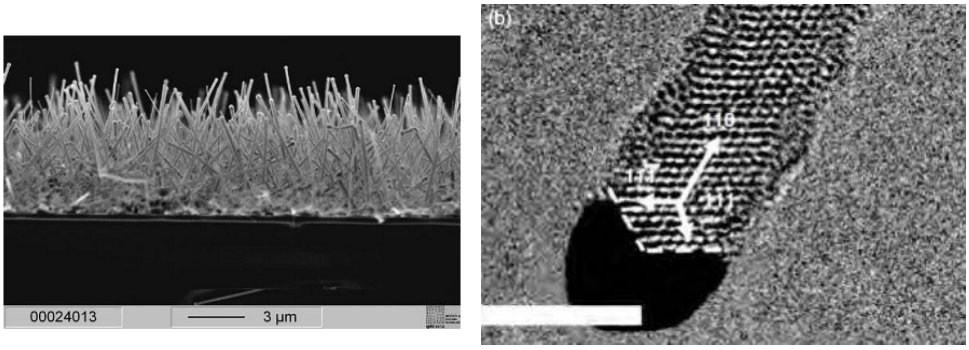

(a) (b)

Fig. 26. (a) SEM image of a Si NW carpet grown from Au nanoparticles (150 nm diameter) on a multicrystalline Si wafer (Andra 2008); (b) HRTEM image of the gold catalyst/nanowire interface of a Si NW with a <110> growth axis. Scale bar is 5 nm (Wu et al., 2004).

4.1.2 Top down approach

In top down approach relies on dimentional reduction through selective etching and various nanoimprinting techniques. For example, well aligned Si NW arrays can be obtained by electroless metal-assisted chemical etching in HF/$AgNO_3$ solution. Basically, a noble metal is deposited on the surface in the form of nanoparticles which act as catalyst for Si etching in HF solution containing an oxidizing agent. As a consequence, the etching only occurs in the vicinity of the metal nanoparticles and results in the formation of well defined mesopores (20-100 nm in diameter (Fang et al., 2008) (Peng et al., 2005) (Fig. 27 (a)).

One of the main advantages of the top – down methods as compared to the bottom –up is that it is possible to start the processing by using conventional wafers with already performed diffusion regions (ex. p^+nn^+) and then etch it into SiNWs. Each nanowire will

thus present the p-n junction already formed. However this method presents some drawbacks. One of them is rather poor size control.
To overcome this problem colloidal crystal patterning combined with metal-assisted etching was applied (Wang et al., 2010) (Wang et al., 2010). The main idea is the next one. The sphere lithography is based on the self-organization of micrometer/nanometer spheres into a monolayer with a hexagonal close-packed structure. Typical material used for the spheres are silica and polystyrene, which are commercially available with narrow size distribution. The deposition of a monolayer of the spheres on a substrate is used as a patterning mask for thin metallic film evaporated on the Si wafer. After the sphere dissolution, the Si surface that comes in contact with the metal is selectively etched, leaving behind an array of Si NWs whose diameter is predefined by the size of holes in the metal film, while the length is determined by the etching time. This method enables the formation of large scale arrays with long – range periodicity of vertically standing nanorods/nanowires with well controlled diameter, length and density (Fig. 27 (b)). It should be however noted that this methods does not permit to achieve SiNWs with the diameters lower than 50 nm and thus potentially cannot be applied for all-Si tandem solar cell.

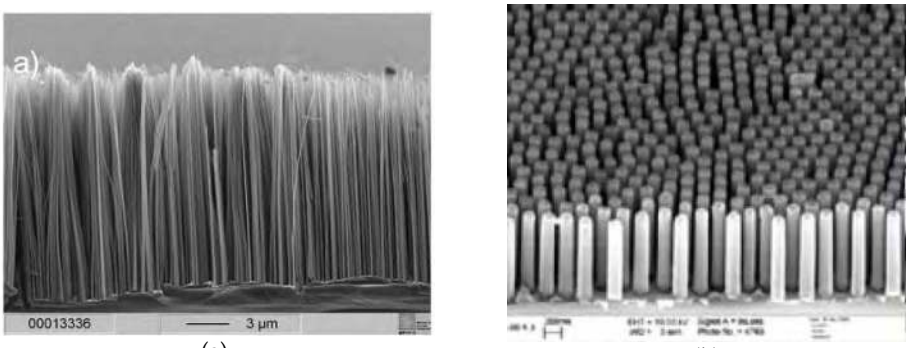

(a) (b)

Fig. 27. SEM images of Si NWs obtained by (a) simple metal-assisted etching technique (Andra 2008) and (b) by colloidal crystal patterning combined with metal-assisted etching approach (Wang et al., 2010).

4.2 Optical properties of Si nanowires

A variety of the optical techniques have shown that the properties of nanowires are different to those of their bulk counterparts, however the interpretation of these measurements is not always straightforward. The wavelength of light used to probe the sample is usually smaller than the wire length, but larger than the wire diameter. Hence, the probe light used in the optical measurement cannot be focused solely onto the nanowire and the wire and the substrate on which the wire rests (or host material if the wire is embedded in a template) are probed simultaneously. For example, for measurements such as photoluminescence, if the substrate does not luminesce or absorb in the frequency range of the measurements, PL measures the luminescence of the nanowire directly and the substrate can be ignored. In reflection and transmission measurements, even a non-absorbing substrate can modify the measured spectra of nanowires. However, despite these technical difficulties it was

experimentally proved that Si nanowire materials have exhibited properties such as ultra-high surface area ratio, low reflection, absorption of wideband light, and tunable bandgap.

4.2.1 Bandgap of quantum SiNWs

In 2003, scanning tunneling spectroscopy measurements on individual oxide-removed Si NWs showed that the optical gap of Si NWs increased with decreasing of Si NW diameter from 1.1 eV for 7 nm to 3.5 eV to 1.3 nm (Ma et al., 2003). Since, a large number of theoretical and experimental works have been done to explore the effect of the chemical passivation, surface reconstruction, cross section geometry and growth orientation on electronic structure of SiNWs (Fernández-Serra et al., 2006) (Yan et al., 2007) (Vo et al., 2006). For example, it was shown than the bandgap of [110] SiNWs is the smallest among those of the [100], [112], and [111] wires of the same diameter (Cui et al., 2000). It should be also noted that the magnitude of the energy increase/decrease in SiNWs induced by quantum confinement is different for each point of the bandstructure. It was predicted that the conduction-band-minimum (CBM) energy increases more near the X point than near the Γ. Therefore for nanowires with sufficiently small dimensions, this difference in the energy shifts at different points in the Brillouin zone is large enough to move the CBM at the X point above the CBM at the Γ point (Vo et al., 2006). Then a transition from an indirect to direct gap material occurs. The indirect to direct transition does not depend on the special cross-sectional shapes and the bandgaps of [110] SiNWs remain direct event for SiNWs with dimensions up to 7 nm. The dependence of the bandgap on SiNW dimension *D* is shown on the Fig. 28 (a). It is obvious that the smaller the dimension of the nanowire the larger the bandgap due to quantum confinement. As *D* decreases from 7 to 1 nm, the bandgap increases from 1.5 to 2.7 eV. In addition to the size dependence, the energy gap also shows significantly different change with respect to the cross-sectional shape. The bandgaps of rectangular and hexagonal SiNWs are rather close while distinctly smaller than that of the triangular SiNWs.

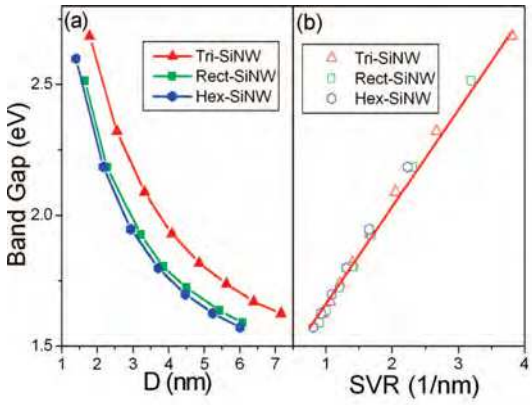

Fig. 28. (a) Bandgap of SiNWs versus the transverse dimension *D*. (b) Bandgap of SiNWs versus SVR (Yao et al., 2008).

The significant cross-sectional shape effects on band gap and size dependence can be understood from the concept of surface –to-volume ratio (SVR). Because of the quantum confinement effect, the band gap increases as the material dimension is reduced, thus

leading to an increase of SVR. In other words, SVR has the impact of enlarging band gap. At the same transverse dimension, triangular SiNW has larger SVR than those of the rectangular SiNW and hexagonal SiNW. As a result, its larger SVR induces the largest band gap among those of the rectangular and hexagonal SiNWs and the strongest size dependence. The bandgap values versus SVR of the SiNWs are shown in Fig. 28 (b). The SVR effect on the bandgap of [110] SiNWs with any cross-sectional shape and area can be described by a universal expression (Yao et al., 2008)

$$E_G\,(eV)=1.28+0.37 \times S\,(nm^{-1}),$$

where S is the value of the SVR in unit of nm^{-1}. The bandgap of SiNWs are usually difficult to measure, but their transverse cross-sectional shape and dimension are easy to know, so it is of significance to predict the bandgap values of SiNWs by using the above expression.

4.2.2 Optical reflection and absorption in SiNWs

Si NW PV devices show improved optical characteristics compared to planar devices. Fig. 29 (a) shows typical optical reflectance spectra of SiNW film as compared to solid Si film of the same thickness (~10μm) (Tsakalakos et al., 2007a). As one can see, the reflectance of the nanowire film is less than 5% over the majority of the spectrum from the UV to the near IR and begins to increase at ~700°nm to a values of ~41% at the Si band edge (1100 nm), similar to the bulk Si. It is clear that the nanowires impart a significant reduction of the reflectance compared to the solid film. More striking is the fact that the transmission of the nanowire samples is also significantly reduced for wavelength greater than ~700°nm (Fig. 29 (b)). This residual absorption is attributed to strong IR light trapping[4] coupled with the presence of the surface states on the nanowires that absorb below bandgap light. However, the level of optical absorption does not change with passivation, which further indicates that light trapping plays a dominant role in the enhanced absorption of the structures at all wavelength. It should be also noted that the absorption edge of a nanowire film shifts to longer wavelength and approaches the bulk value as the nanowire density is increased. Essentially, the Si nanowire arrays act as sub-wavelength cylindrical scattering elements, with the mactroscopic optical properties being dependent on nanowire pitch, length, and diameter.

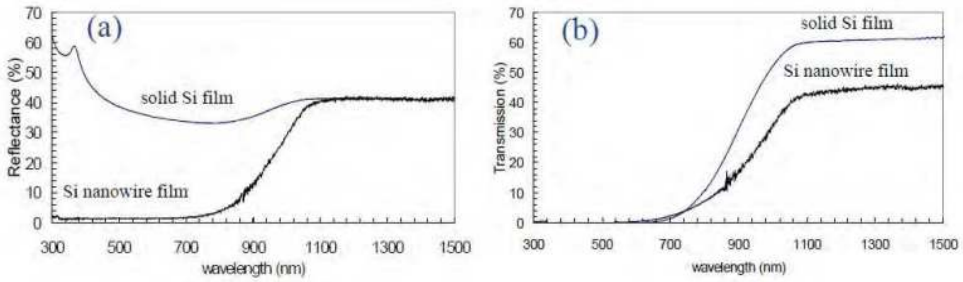

Fig. 29. Total (a) reflectance and (b) transmission data from integrated sphere measurements for 11 μm thick solid Si film and nanowire film on glass substrate (Tsakalakos et al., 2007).

[4] Light trapping is typically defined as the ratio of the effective path length for light rays confined within a structure with respect to its thickness.

4.3 Electrical transport in SiNWs

Important factors that determine the transport properties of Si nanowires include the wire diameter (important for both classical and quantum size effect), surface conditions, crystal quality, and the crystallographic orientation along the wire axis (Ramayya et al., 2006) (Duan et al., 2002).

Electronic transport phenomena in Si nanowires can be roughly divided into two categories: ballistic transport and diffusive transport. Ballistic transport phenomena occur when the electrons can travel across the nanowire without any scattering. In this case the conduction is mainly determined by the contact between the nanowire and the external circuit. Ballistic transport phenomena are usually observed in very short quantum wires. On the other hand, for nanowires with length much larger than the carrier mean free path, the electrons (or holes) undergo numerous scattering events when they travel along the wire. In this case, the transport is in the diffusive regime, and the conduction is dominated by carrier scattering within the wires, due to lattice vibrations, boundary scattering, lattice and other structural defects and impurity atoms.

The electronic transport behavior of Si nanowires may be categorized based on the relative magnitudes of three length scales: carriers mean free path, the de Broglie wavelength of electrons, and the wire diameter. For wire diameters much larger than the carrier mean free path, the nanowiers exhibit transport properties similar to bulk materials, which are independent of the wire diameter, since the scattering due to the wire boundary is negligible, compared to other scattering mechanisms. For wire diameters comparable or smaller than the carrier mean free path, but still larger than the de Broglie wavelength of the electrons, the transport in the nanowire is in the classical finite regime, where the band structure of the nanowire is still similar to that of the bulk, while the scattering events at the wire boundary alter their transport behavior. For wire diameters comparable to electronic wavelength (de Broglie wavelength of electrons), the electronic density of states is altered dramatically and quantum sub-bands are formed due to quantum confinement effect at the wire boundary. In this regime, the transport properties are further influenced by the change in the band structure. Therefore, transport properties for nanowires in the classical finite size and quantum size regimes are highly diameter-dependent. Experimentally it was shown that the carrier mobility in SiNWs can reach that one in bulk Si at a doping concentration of 10^{20} cm^{-3} and decreases for smaller diameter wires (Cui et al., 2000).

Because of the enhanced surface-to-volume ratio of the nanowires, their transport behavior may be modified by changing their surface conditions. For example, it was shown on the n-InP nanowires, that coating of the surface of these nanowires with a layer of redox molecules, the conductance may be changed by orders of magnitude (Duan et al., 2002).

4.4 Comparison of axial and radial p-n junction nanowire solar cells

Independently of the nanowire preparation method two designs of NW solar cells are now under consideration with p-n junction either radial or axial (Fig. 30). In the radial case the p-n junction covers the whole outer cylindrical surface of the NWs. This was achieved either by gas doping or by CVD deposition of a shell oppositely doped to the wire (Fang, 2008) (Peng, 2005) (Tian 2007). In the axial variant, the p-n junction cuts the NW in two cylindrical parts and require minimal processing steps (Andra 2008). However, solar cells that absorb photons and collect charges along orthogonal directions meet the optimal relation between the absorption values and minority charge carrier diffusion lengths (Fig. 30 (a)) (Hochbaum 2010). A solar cell consisting of arrays of radial p-n junction nanowires (Fig. 30 (b)) may

provide a solution to this device design and optimization issue. A nanowire with a p-n junction in the radial direction would enable a decoupling of the requirements for light absorption and carrier extraction into orthogonal spatial directions. Each individual p-n junction nanowire in the cell could be long in the direction of incident light, allowing for optimal light absorption, but thin in another dimension, thereby allowing for effective carrier collection.

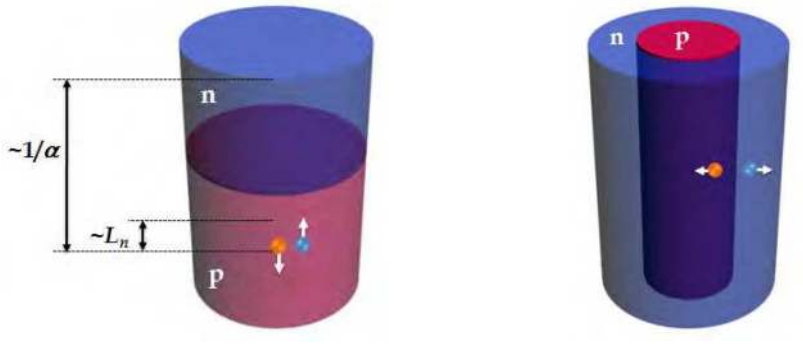

(a) (b)

Fig. 30. Schematic views of the (a) axial and (b) radial nanowire solar cell. Light penetration into the cell is characterized by the optical thickness of the material (α is the absorption coefficient), while the mean free path of generated minority carriers is given by their diffusion length. In the case of axial nanowire solar cell, light penetrates deep into the cell, but the electron-diffusion length is too short to allow the collection of all light-generated carriers (Kayes et al., 2005).

The comparison between the axial and radial p-n junction technologies for solar cell applications was performed in details in Ref (Kayes et al., 2005). In the case of radial p-n junction, the short-circuit current (I_{sc}) increases with the nanowire length and plateaus when the length of the nanowire become much greater than the optical thickness of the material. Also, I_{sc} was essentially independent on the nanowire radius, provided that the radius (R) was less than the minority carrier diffusion length (L_n). However, it decreases steeply when $R > L_n$. I_{sc} is essentially independent of trap density in the depletion region. Being rather sensitive to a number of traps in the depletion region, the open circuit voltage V_{oc} decreases with increasing nanowire length, and increases with nanowire radius. On the other hand the trap density in the quasineutral regions had relatively less effect on V_{oc}. The optimal nanowire dimensions are obtained when the nanowire has a radius approximately equal to L_n and a length that is determined by the specific tradeoff between the increase in I_{sc} and the decrease in V_{oc} with length. In the case of low trap density in the depletion region, the maximum efficiency is obtained for nanowires having a length approximately equal to the optical thickness. For higher trap densities smaller nanowire lengths are optimal.
Radial p-n junction nanowire cells trend to favor high doping levels to produce high cell efficiencies. High doping will lead to decreased charge-carrier mobility and a decreased depletion region width, but in turn high doping advantageously increases the build-in voltage. Because carriers can travel approximately one diffusion length through a quasineutral region before recombining, making the nanowire radius approximately equal

to the minority –electron diffusion length allows carriers to traverse the cell even if the diffusion length is low, provided that the trap density is relatively low in the depletion region.

An optimally designed radial p-n junction nanowire cell should be doped as high as possible in both n- and p- type regions, have a narrow emitter width, have a radius approximately equal to the diffusion length of the electrons in the p-type core, and have a length approximately equal to the thickness of the material. It is crucial that the trap density near the p-n junction is relatively low. Therefore one would prefer to use doping mechanisms that will getter impurities away from the junction. By exploiting the radial p-n junction nanowire geometry, extremely large efficiency gains up to 11% are possible to be obtained.

4.5 Fabrication of Si QD PV devices

By using VLS method (Tian et al., 2007) (Kelzenberg et al., 2008) (Rout et al., 2008) (Fang et al., 2008) (Perraud et al., 2009) as well as by the etching method (Garnett et al., 2008) (Peng et al., 2005). SiNW based photovoltaic devices were experimentally demonstrated. Nearly all the works were concerned with Si wafers as a substrate. However, it should be noted that for competitive solar cells, low cost substrates, such as glass or metal foils are to be preferred. Schematic view of the VLS fabricated structure of the SiNW array solar cells is illustrated on Fig. 31 (a). The n-type SiNWs were prepared by the VLS method on (100) p-type Si substrate (14-22 Ωcm). Device fabrication started from the evaporation of 2-nm thick gold film followed by annealing at 550°C for 10 min under H_2 flow to form Au nanocatalyzers. SiNWs were subsequently grown at 500° with SiH_4 diluted in H_2 as the gas precursor. N-type doping was achieved by adding PH_3 to SiH_4, with PH_3/SiH_4 ratio of $2x10^{-3}$ corresponding to a nominal phosphorous density of $10^{20}cm^{-3}$. After the VLS growth the gold catalysts were etched off in KI/I_2 solution, and the doping impurities were activated by rapid thermal annealing at 750° for 5 min. The SiNW array was then embedded into spin-on-glass (SOG) matrix. Indeed, SOG matrix ensures a good mechanical stability of the SiNW array and enables further processing steps, such as front surface planarization and electrical contact deposition. The planarization step is normally performed by the chemical-mechanical polishing. To form the front contacts indium-tin-oxide (ITO) was firstly deposited on planarized SOG surface followed by the deposition of Ni/Al contact grid. As back electrical contact, the sputtered and annealed Al was used. The area of the fabricated SiNW solar cell was 2.3 cm^{-2}.

The sheet resistance of n-type SiNWs embedded into SOG matrix was estimated to be 10^{-4} Ω/sq. I-V measurements in the dark and under 1-sun illumination (Fig. 31 (b)) indicate a good rectifying junction. The measured I_{SC}, V_{OC} and FF were 17 mA/cm^2, 250mV and 44%, respectively, leading to an energy-conversion efficiency of 1.9%. The V_{OC} of Si NW solar cell was shown to be increased up to 580 mV (Peng et al., 2005). The parasitic series resistance found for SiNW solar cells (~5 Ω cm^{-2}) was slightly larger than in the standard 1st generation solar cells (~2 Ω cm^{-2}), however the p-n junction reverse current was of the order of 1 $\mu A/cm^2$ with is about 100 times bigger than in typical Si solar cells (~1 pA/cm^2). Such a high pn junction reverse current indicates a high density of localized electronic states within the bandgap, which act as generation-recombination centers. These states may come from contamination of Si by gold which is used as catalyst for VLS growth. Other types of metallic catalysers, like Sn, were also used (Uchiyama et al., 2010).

However, for a moment by using this catalyzer it is difficult to achieve the diameter of SiNWs less that 200 nm. The electronic states in the bandgap may also come from a lack of passivation of surface defects. The passivation step is rather crucial for SiNW solar cells, since SiNW have very high SVR ratio and their opto-electronic properties strongly depends on the surface passivation.

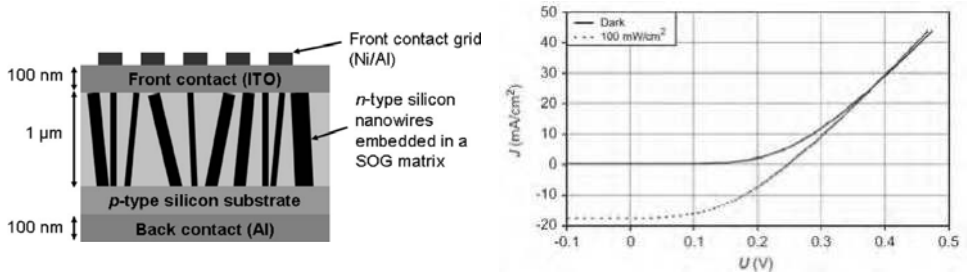

(a) (b)

Fig. 31. (a) Structure of the SiNW array solar cell. A p-n junction is formed between the n-type SiNWs and the p-type Si substrate; (b) Dark and illuminated I-V measurements of n-type SiNWs on p-type Si substrate (Perraud et al., 2009).

The theoretical value of the efficiency for Si nanowire solar cells is predicted to be as high as 16%, which makes them perfect candidates for higher bandgap bricks in all-Si tandem cell approach. The first prototypes of SiNW solar cells have excellent antireflection capabilities and shown the presence of the photovoltaic effect. However, up today there was no evidence that this photovoltaic effect occurred in a material with an increased bandgap.

5. Conclusions

Silicon based third generation photovoltaics is a quickly developing field, which integrates the knowledge from material science and photovoltaics. Today the first prototypes of both Si QD solar cells and Si NWs solar cells have already been developed. For a moment they present V_{OC}, I_{SC} and FF values which still lower than those ones of the 1st generation PV cells based on bulk Si – but all these problems are being addressed. It is too prematurely to draw the conclusions while the further optimization steps of the fabrication parameters were not performed. We should not forget that, for example, although the airplane was not invented until the early 20th century, Leonardo da Vinci sketched a flying machine four centuries earlier.

6. References

Abeles, B.; Pinch, H. L. & Gittleman, J. I. (1975), Percolation conductivity in W-Al_2O_3 granular metal films, *Phys. Rev. Lett.*, Vol. 35, pp. 247-250.

Aeberhard, U. (2011), Theory and simulation of photogeneration and transport in Si-SiOx superlattice absorbers, *Nanoscale Research Letters*, Vol. 6, p. 242.

Allan, G. & Delerue, C. (2007), Energy transfer between semiconductor nanocrystals: Validity of Förster's theory, *Phys. Rev. B*, Vol. 75, pp. 195311.

Andra, G.; Pietsch, M.; Sivakov, V.; Stelzner, Th.; Gawlik, A.; Christiansen, S.& Falk, F. (2008). Thin film solar cells based on single crystalline silicon nanowires, *Proceedings of 23th European Photovoltaic Solar Cell Energy Conference*., Spain, pp. 163-167

Antonova, A.; Gulaev, M.; Savir, E.; Jedrzejewski, J, & Balberg, I. (2008), Charge storage, photoluminescence, and cluster statistics in ensembles of Si QDs, *Phys. Rev. B*., Vol. 77, pp. 123318.

Balberg, I,; Azulay, D.; Toker, D. & Millo, O. (2004), Percolation and tunneling in composite materials, *Int. J. Mod. Phys. B*, Vol. 18, pp. 2091-2121.

Balberg, I.; Savir, E.; Jedrzejewski, J, Nassiopoulou, A. & Gardelis, S. (2007), Fundamental transport processes in ensembles of silicon quantum dots, *Phys. Rev. B*., Vol. 75, pp. 235329.

Balberg, I. (2010) Chapter 4, in *Silicon Nanocrystals: Fundamentals, Synthesis and Application* (ed. L. Pavesi and R; Turan), Wiley, Weinheim.

Ball, J. & Reehal, H. (2010), The effect of substrate bias on the growth of silicon nanowires from Tin catalyst layers,, *Proceedings of 25th European Photovoltaic Solar Cell Energy Conference*, Spain, September 6-10, pp. 769-772.

Bulutay,C. (2007), Electronic structure and optical properties of silicon nanocrystals along their aggregation stages , *Physica E*, Vol. 38, pp. 112.

Bulutay, C. & Ossicini, S. (2010) Chapter 2, in *Silicon Nanocrystals: Fundamentals, Synthesis and Application* (ed. L. Pavesi and R; Turan), Wiley, Weinheim.

Canham, L. T. (1990), Silicon quantum wire array fabrication by electrochemical and chemical dissolution of wafers, *Appl. Phys. Lett.*, Vol. 57, pp. 1046.

Cho, E-Ch,; Green, M.; Xia, J.; Corkish, R.; Reece, P.; & Gal, M (2004), Clear quantum-confined luminescence from silicon/SiO_2 single quantum wells, *Appl. Phys. Lett.*, Vol. 84, p. 2286.

Cho, Y. H.; Green, M. A.; Cho, E-Ch.; Huang, Yu.; Trupke, Th. & Conibeer, G. (2005), Silicon quantum dots in SiNx matrix for third generation photovoltaics, *Proceedings of 20th European Photovoltaic Solar Cell Energy Conference*, Spain, June 6-10, pp. 47-50

Cho, E.C.; Green, M.A.; Conibeer, G.; Song, D.Y.; Cho, Y.H.; Scardera, G.; Huang, S.J.; Park, S.; Hao, X.J.; Huang, Y. & Dao, L.V. (2007) Silicon quantum dots in a dielectric matrix for all-silicon tandem solar cells. *Adv. OptoElectr.*, 2007, Article ID 69578.

Conibeer, G.; Green, M.; Cho, Cho, Eu-Ch.; König, D.; Cho, Y-H.; Fangsuwannarak, T.; Scardera, G.; Pink, E.; Huang, Yi.; Puzzer, T.; Huang, Sh.; Song, D.; Flynn, Ch.; Park, S.; Hao, X.& Mansfield, D. (2008), Silicon quantum dot nanostructures for tandem photovoltaic cells, *Thin Solid Films*, Vol. 516, pp. 6748-6756.

Conibeer, G. (2010) Chapter 20, in *Silicon Nanocrystals: Fundamentals, Synthesis and Application* (ed. L. Pavesi and R; Turan), Wiley, Weinheim.

Conibeer, G.; Green, M.; König, D.; Perez-Wurfl, I.; Huang, S.; Hao, X.; Di, D.; Shi, L.; Shrestha, S.; Puthen-Veetil, B.; So, Y.; Zhang, B. & Wan, Z. (2010a), Silicon quantum dot based solar cells: addressing the issues of doping, voltage and current

transport, *Proceedings of 25th European Photovoltaic Solar Cell Energy Conference*, Spain, September 6-10, pp. 182-190.

Crisp, D.; Pathare, A. & Ewell, R.C. (2004), The performance of gallium arsenide/germanium solar cells at the Martian surface, *Acta Astronautica,* Vol. 54, pp. 83-101.

Cui, Y.; Duan, X.; Hu, J. & Lieber, C.M., (2000), Doping and electrical transport in Si nanowires, *J. Phys. Chem. B* Vol. 104, pp. 5213-5216.

Cui Y., & Lieber, C.M. (2001), Functional Nanoscale Electronic Devices Assembled Using Silicon Nanowire Building Blocks, *Science* Vol. 291, pp. 851-853.

Cui, Y.; Lauhon, L.J.; Gudiksen, M.S.; Wang J. & Lieber, C.M. (2001a), Diameter-controlled synthesis of single-crystal silicon nanowires, *Appl. Phys. Lett.* Vol. 78, pp. 2214

Degoli, E.; Luppi, M. & Ossicini, S. (2000), From Undulating Si Quantum Wires to Si Quantum Dots: A Model for Porous Silicon, *Phys. Stat. Solidi (a)*, Vol. 182, pp. 301

Di. D.; Perez-Wurfl, I.; Conibeer, G. & Green, M. (2010) Formation and photoluminescence of Si quantum dots in SiO_2/Si_3N_4 hybrid matrix for all-Si tandem solar cells, *Sol. Energy Mater. Sol. Cells*. Vol. 94, pp. 2238-2243.

Duan, X.; Huang, Y. & Lieber, C. (2002) Nonvolatile memory and programmable logic from molecule-gated nanowires, Nano Lett., Vol. 2, pp. 487-490.

Erwin, S.C.; Zu, L.J.; Haftel, M.I.; Efros, A.L.; Kennedy, T.A.; & Norris, D.J. (2005) Doping semiconductor nanocrystals. *Nature*, Vol. 436, pp.91–94.

Fang, H.; Li, X.; Song, S.; Xu, Y. & Zhu, J. (2008), Fabrication of slantingly-aligned silicon nanowire arrays for solar cell applications, *Nanotechnology,* Vol. 19, pp.255703

Fangsuwannarak, T. (2007) Electronic and optical characterisations of silicon quantum dots and its applications in solar cells, PhD Thesis, University of New South Wales, Australia.

Fernández-Serra, M.; Adessi, Ch. & Blasé, X. (2006) Conductance, Surface Traps, and Passivation in Doped Silicon Nanowires, *Nano Lett.* Vol. 6, pp. 2674-2678.

Ficcadenti, M.; Pinto, N.; Morresi, L.; Murri, R.; Serenelli, L.; Tucci, M.; Falconieri, M.; Krasilnikova Sytchkova, A.; Grilli, M.L.; Mittiga, A.; Izzi, M.; Pirozzi, L. & Jadkar, S.R. (2009) Si quantum dots for solar cell fabrication, *Materials Science and Engineering B*, Vol. 159-160, pp. 66-69.

Fujii, M.; Hayashi, S.; & Yamamoto, K. (1998) Photoluminescence from B-doped Si nanocrystals. *J. Appl. Phys.,* Vol. 83, pp. 7953–7957

Fujii, M.; Mimura, A.; Hayashi, S.; Yamamoto, K.; Urakawa, C.; & Ohta, H. (2000) Improvement in photoluminescence efficiency of SiO_2 films containing Si nanocrystals by P doping: an electron spin resonance study. *J. Appl. Phys.*, Vol. 87, pp. 1855–1857.

Fujii, M.; Mimura, A.; Hayashi, S.; Yamamoto, Y.; & Murakami, K. (2002) Hyperfine structure of the electron spin resonance of phosphorus-doped Si nanocrystals. *Phys. Rev. Lett.,* Vol. 89, pp. 206805.

Fujii, M. (2010) Chapter 3, in *Silicon Nanocrystals: Fundamentals, Synthesis and Application* (ed. L. Pavesi and R; Turan), Wiley, Weinheim.

Fukata, N. (2009), Impurity doping in silicon nanowires, *Adv. Mater*. Vol. 21, pp. 2829-2832.

Garnett, E. & Yang, P. (2008) Silicon Nanowire Radial p−n Junction Solar Cells, *J. Am. Chem. Soc.* Vol. 130, pp.9224-9225.

Gradmann, R.; Löper, Ph.; Künle M.; Rothfelder, M.; Janz, S.; Hermle, M.& Glunz, S. (2010), Silicon nanocrystals in SiC: the influence of doping on crystallization and electrical properties, *Proceedings of 25th European Photovoltaic Solar Cell Energy Conference*, Spain, September 6-10, pp. 199-202.

Green, M. (2002), Third generation photovoltaics: solar cells for 2020 and beyond, *Physica E*, Vol. 14, pp. 65-70.

Green, M. (2003). *Third generation photovoltaics (advanced solar energy conversation)*, Springer, pp.160.

Green, M. A.; Cho, E.-C.; Huang, Y.; Pink, E.; Trupke, T.; Lin, A.; Fangsuwannarak T.; Puzzer, T.; Conibeer, G. & Corkish, R. (2005), All-Si tandem cells based on "artificial" semiconductor synthesized using silicon quantum dots in dielectric matrix , *Proceedings of 20th European Photovoltaic Solar Cell Energy Conference*, Spain, June 6-10, pp. 3-7

Green, M. A.; Conibeer, G.; Cho, E.-C.; König, D.; Huang, S.; Song, D.; Scardera, G.; Cho, Y.; Hao, X.; Fangsuwannarak T.; Park, S. W.; Perez-Wurfl, P.; Huang, Y.; Chang, S.; Pink, E.; Bellet, D.; Bellet-Almaric, E. & Puzzer, T. (2007), Progress with Si-based tandem cells using quantum dots in dielectric matrix, *Proceedings of 22th European Photovoltaic Solar Cell Energy Conference*, Italy, September 3-7, pp. 1-4

Green, M.; Emery, K.; Hishikawa, Y. & Warta, W. (2010), Solar cell efficiency tables (version 36), *Progress in photovoltaics: research and applications*, Vol. 18, pp. 346-352.

Hao, X.J.; Cho, E.-C.; Scardera, G.; Shen, Y.S.; Bellet-Amalric, E.; Bellet, D.; Conibeer, G.; & Green, M.A. (2009) Phosphorus doped silicon quantum dots for all-silicon quantum dot tandem solar cells. *Sol. Energy Mater. Sol. Cells*, Vol. 93, pp. 1524.

Hao, X.J.; Cho, E-C.; Flynn, C.; Shen, Y.S.; Park, S.C.; Conibeer, G. & Green, M. (2009a), Synthesis and characterization of boron-doped Si quantum dots for all-Si quantum dot tandem solar cells, *Sol. Energy Mater. Sol. Cells*, Vol. 93, pp. 273-279.

Holtz, P.O. & Zhao, Q.X. (2004) Impurities Confined in Quantum Structures, Springer-Verlag, Berlin.

Huynh, W.; Dittmer, J. & Alivisatos, A. (2002) Hybrid nanorod-polymer solar cells, *Science*, Vol. 295, pp. 2425-2427.

Jiang Ch. & Green. M. (2006), Silicon quantum dot superlattices: modeling of energy bands, densities of states and mobilities for silicon tandem solar cell applications, *J. Appl. Phys.*, Vol. 99, p. 114902.

Jie, J. S.; Zhang, W. J.; Jiang, Y.; Meng, X. M.; Li, Y. Q. & Lee S. T. (2006), Photoconductive Characteristics of Single-Crystal CdS Nanoribbons, *Nano Lett.* Vol. 6, pp. 1887-1892.

Kayes, B.; Atwater, H. & Lewis, N. (2005), Comparison of the device physics principles of planar and radial p-n junction nanorod solar cells, *J. Appl. Phys.*, Vol. 97, pp. 114302.

Kelzenberg, M.; Turner-Evans, D.; Kayes, B.; Filler, M.; Putnam, M.; Lewis, N. & Atwater, H. A. (2008), Photovoltaic Measurements in Single-Nanowire Silicon Solar Cells, *Nano Lett.* Vol. 8, pp. 710-714.

Kim, T.; Park, N.; Kim, K.; Yong Sung, G.; Ok, Y.; Seong, T. &, Choi, Ch. (2004), Quantum confinement effect of silicon nanocrystals in situ grown in silicon nitride films, *Appl. Phys. Lett.*, Vol. 85, pp. 5355.

Kim, B.H., Cho, C., Kim, T., Park, N., Sung, G., and Park, S. (2005) Photoluminescence of silicon quantum dots in silicon nitride grown by NH3 and SiH4. *Appl. Phys. Lett.,* 86, 091908., idem

Kim, T.-W.; Cho, Ch-H,; Kim, B-H, & Park, S-Ju. (2006), Quantum confinement effect in crystalline silicon quantum dots in silicon nitride growth using SiH_4 and NH_3, *Appl. Phys. Lett.*, Vol. 88, p. 123102.

König, D.; Rudd, J.; Green, A. & Conibeer, G. (2009) Impact of interface on the effective bandgap of Si quantum dots, *Sol. Energy Mater. Sol. Cells*, Vol. 93, pp. 753-758.

Kovalev, D.; Heckler, H.; Ben-Chorin, M.; Polisski, G.; Schwartzkopff, M. & Koch, F. (1998) Breakdown of the k-conservation rule in Si nanocrystals. *Phys. Rev. Lett.,* Vol. 81, pp. 2803–2806.

Kovalev, D.; Heckler, H.; Polisski, G.; & Koch, F. (1999) Optical properties of Si nanocrystals. *Phys. Status Solidi B*,Vol. 215, pp. 871–932.

Kovalev, D. & Fujii, M. (2008) Chapter 15, in *Silicon Nanophotonics: Basic Principles, Present Status and Perspectives* (ed. L. Khriachtchev), World Scientific, Singapore.

Kurokawa, Y.; Miyajima, S.; Yamada, A.& Konagai, M. (2006) Preparation of nanocrystalline silicon in amorphous silicon carbide matrix, *Jpn. J. Appl. Phys.* Vol. 45, pp. L1064-L1066.

Law, M.; Greene, L.; Johnson, J.; Saykally, R. & Yang P. (2005), Nanowire dye-sensitiezed solar cells, *Nat. Mater,* Vol. 4, pp. 455-459.

Lazarenkova, O. & Balandin, A. (2001), Miniband formation in a quantum dot crystal, *J. Appl. Phys.*, Vol. 89, p. 5509.

Lelièvre, J.-F.; De la Torre, J.; Kaminski, A.; Bremond, G.; Lemiti, M.; El Bouayadi, R.; Araujo, D.; Epicier, T.; Monna, R.; Pirot, M.; Ribeyron, P.-J. & Jaussaud, C. (2006), Correlation of optical and photoluminescence properties in amorphous SiNx:H thin films deposited by PECVD or UVCVD, *Thin Solid Films*, Vol. 511-512, pp. 103-107

Lenahan, P.M. & Conley, J.F. (1998) What can electron paramagnetic resonance tell us about the Si/SiO2 system? *J. Vac. Sci. Technol. B*, Vol. 16, pp. 2134–2153.

Lockwood, D. J.& Tsybeskov, L. (2004) Nanocrystalline Silicon Superlattices, in *Encyclopedia of Nanoscience and Nanotechnology* (ed. By H. S. Nalwa), Vol. 6, pp. 477-494.

Löper, P.; Hiller, D.; Künle, M.; Grandmann, R.; Rothfelder, M.; Janz, S.; Hermle, M.; Zacharias, M. & Glunz, S. W. (2010), Carrier confinement and transport in high band gap materials with embedded Si QDs, *Proceedings of 25th European Photovoltaic Solar Cell Energy Conference*, Spain, September 6-10, pp. 269-273

Ma, D.; Lee, C. S.; Au, F.; Tong, S. & Lee, S. T. (2003), Small-Diameter Silicon Nanowire Surfaces, *Science*, Vol. 299, pp. 1874-1877.

Marti, A. & Araujo, A. (1996) Limiting efficiencies for photovoltaic energy conversion in multigap systems, *Sol. Energy Mater. Sol. Cells*. Vol. 43, pp. 203-222.

Meillaud, F.; Shah, A.; Droz, C.; Vallat-Sauvain, E. & Miazza, C. (2006) Efficiency limits for single-junction and tandem solar cells, *Sol. Energy Mater. Sol. Cells*. Vol. 90, pp. 2952-2959.

Mercaldo, L.; Veneri, P.; Esposito, E. & Fameli, G. (2010), Micro-raman investigation of silicon nitride embedding Si nanostructures, *Proceedings of 25th European Photovoltaic Solar Cell Energy Conference*, Spain, September 6-10, pp. 223-228.

Mimura, A.; Fujii, M.; Hayashi, S.; & Yamamoto, K. (1999) Quenching of photoluminescence from Si nanocrystals caused by boron doping. *Solid State Commun.,* Vol. 109, pp.561–565.

Mimura, A.; Fujii, M.; Hayashi, S.; Kovalev, D. & Koch, F. (2000) Photoluminescence and free-electron absorption in heavily phosphorous – doped si nanocrystals, *Phys. Rev. B*., Vol. 62, p. 12625-12627.

Mitin, V. (2010), Quantum mechanics for nanostructures, Cambridge University Press, p. 431.

Müller, J.; Finger, F.; Carius, R.; & Wagner, H. (1999) Electron spin resonance investigation of electronic states in hydrogenated microcrystalline silicon. *Phys. Rev. B*, Vol. 60, p.11666.

Nelson, J. (2003). *The physics of solar cells,* Imperial College, *UK*, pp.384.

Norris, D.J.; Efros, A.L., & Erwin, S.C. (2008) Doped nanocrystals. *Science*, Vol. 319, pp. 1776–1779.

Nychyporuk, T.; Marty, O.; Rezgui, B.; Sibai, A.; Lemiti, M. & Bremond, G. (2008), Towards the 3rd generation photovoltaics: absorption properties of silicon nanocrystals embedded in silicon nitride matrix, *Proceedings of 23th European Photovoltaic Solar Cell Energy Conference*, Spain, September 1-5, pp. 491-494.

Nychyporuk, T.; Zakharko, Yu.; Lysenko, V. & Lemiti, M. (2009), Interconnected Si nanocrystals forming thin films with controlled bandgap values, *Appl. Phys. Lett.*, Vol. 95, pp. 083124.

Nychyporuk, T.; Zhou, Z.; Fave, A.; Lemiti, M. & Bastide, S. (2010) Electroless deposition of Ag nanoparticles on the surface of SiN_x:H dielectric layers, *Sol. Energy Mater. Sol. Cells*, Vol. 94, pp. 2314-2317.

Ögüt, S. & Chelikowsky, J. R. (1997), Quantum confinement and optical gaps in Si nanocrystals, *Phys. Rev. Lett.*, Vol. 79, pp. 1770-1773.

Ossicini, S.; Degoli, E.; Iori, F.; Luppi, E.; Magri, R.; Cantele, G.; Trani, F. & Ninno, D. (2005), Simultaneously B- and P- doped silicon nanoclusters: formation energies and electronic properties, *Appl. Phys. Lett.*, Vol. 87, p. 173120.

Ossicini, S.; Iori, F.; Degoli, E.; Luppi, E.; Magri, R.; Poli, R.; Cantele, G.; Trani, F. & Ninno, D. (2006) Understanding doping in silicon nanostructures. *IEEE J. Sel. Top. Quant.*, Vol. 12, pp. 1585–1591.

Park, N.; Choi, Ch.; Seong, T. & Park, S. (2000), Quantum confinement in amorphous Si quantum dots embedded in silicon nitride, *Phys. Rev. Lett.*, Vol. 86, p. 1355.

Peng, K.; Xu,; Y. Wu,; Y.; Yan, Y.; Lee, S. & Zhu, J. (2005), Aligned Single-Crystalline Si Nanowire Arrays for Photovoltaic Applications, *Small*, Vol. 1, pp. 1062-1067.

Perraud, S.; Poncet, S.; Noël, S.; Levis, M.; Faucherand, P.; Rouvière, E.; Thony, P.; Jaussaud, C. & Delsol, R. (2009), Full process for integrating silicon nanowire arrays into solar cells, *Sol. Energy Mater. Sol. Cells*, Vol. 93, pp. 1568-1571.

Pi, X.; Gresback, R.; Liptak, R. W. & Krtshagen, U. (2008), Doping efficiency, dopant location, and oxidation of Si nanocrystals, *Appl. Phys. Lett.*, Vol. 92, p. 123102.

Raisky, O.Y.; Wang, W.B; Alfano, R.R.; Reynolds, C.L.; Stampone, D.V. & Focht, M.W. (1999) Resonant enhancement of the photocurrent in multiple-quantum-well photovoltaic devices, *Appl. Phys. Lett.*, Vol. 74, pp. 129.

Ramayya, E.; Vasileska, D.; Goodnick, S. & Knezevic, I. (2006), Electron transport in Si nanowires, *Journal of Physics: Conference Series*, Vol. 38, pp. 126-129.

Reeves, G. K. & Harrison, H. B. (1982) Contact resistance of polysilicon silicon interconnections, Electronic Letters, Vol. 18, pp. 1083-1085.

Rout, Ch. & Rao, C. N. R. (2008), Electroluminescence and rectifying properties of heterojunction LEDs based on ZnO nanorods, *Nanotechnology,* Vol. 19, pp.285203

Scardera, G.; Puzzer, T.; Perez-Wurfl, I. & Conibeer, G. (2008) The effects of annealing temperature on the photoluminescence from silicon nitride multilayer structures. *J. Crystal Growth*, Vol. 310, pp. 3680–3684.

Shockley, W. & Queisser, H. J. (1961), Detailed balance limit of efficiency of p-n junction solar cells, *J. Appl. Phys.*, Vol. 32, p. 510.

Sinke, W.C.; del Canizo, C. & del Coso G. (2008). 1 € per Watt-peak advanced crystalline silicon modules: the Crystal Clear integrated project, *Proceedings of 25th European Photovoltaic Solar Cell Energy Conference*, Spain, pp.3700-3705.

So, Y. H.; Perez-Wurfl, I.; Shi, L;; Huang, S;; Conibeer, G. & Green, M. (2010), Silicon nitride as alternative matrix for all-Si tandem solar cell, *Proceedings of 25th European Photovoltaic Solar Cell Energy Conference*, Spain, September 6-10, pp. 690-692.

Song, D.; Cho, Eu-C.; Conibeer, G.; Huang, Yi.; Flynn, Ch. & Green, M. A. (2008), Structural characherization of annealed $Si_{1-x}C_x$/SiC multilayers targeting formation of Si nanocrystals in a SiC matrix, *J. Appl. Phys*, Vol. 103, p. 083544

Song, D.; Cho, E.-C.; Conibeer, G. & Green M. (2009) Solar cells based on Si-NCs embedded in a SiC matrix, Technical Digest of the 18th International Photovoltaic Science and Engineering Conference, India, 19-23 January.

Stegemann, B.; Lussky, T.; Schöpke, A.; Cermak, J.; Rezek, B.; Kocka, J. & Schmidt, M. (2010), Formation kinetics and electrical transport of silicon quantum dot layers, *Proceedings of 25th European Photovoltaic Solar Cell Energy Conference*, Spain, September 6-10, pp. 260-264.

Stegner, A.R.; Pereira, R.N.; Klein, K.; Lechner, R.; Dietmueller, R.; Brandt, M.S.; Stutzmann, M. & Wiggers, H. (2008) Electronic transport in phosphorus-doped silicon nanocrystal networks. *Phys. Rev. Lett.*, Vol. 1, p. 026803.

Surana, K.; Lebrun, J. M.; Lepage, H.; Doisneau, B.; Vellet, D.; Le Carval, G.; Thony, P. & Mur, P. (2010), Enhanced conduction in Si QD superlattice in SiO_2 matrix, *Proceedings of 25th European Photovoltaic Solar Cell Energy Conference*, Spain, September 6-10, pp. 654-656.

Tae-Wook Kim, Chang-Hee Cho, Baek-Hyun Kim, and Seong-Ju Park, Quantum confinement effect in crystalline silicon quantum dots in silicon nitride grown using SiH4 and NH3, *Appl. Phys. Lett.*, Vol. 88, pp. 123102. Idem

Takeoka, S.; Fujii, M.; & Hayashi, S. (2000) Size-dependent photoluminescence from surface-oxidized Si nanocrystals in a weak confinement regime. *Phys. Rev. B*, Vol. 62, pp. 16820–16825.

Tchebotareva, A.L.; Dooda, M.J.A.d.; Biteenb, J.S.; Atwaterb, H.A. & Polman, A. (2005) Quenching of Si nanocrystal photoluminescence by doping with gold or phosphorous. *J. Lumin.*, Vol. 114, pp. 137–144.

Tian, B.; Zheng, X.; Kempa, T.; Fang, Y.; Yu, N.; Yu, G.; Huang, J. & Lieber, C. M. (2007), Coaxial silicon nanowires as solar cells and nanoelectronic power sources, *Nature*, Vol. 449, pp. 885-890.

Tsakalakos, L.; Balsh, J.; Fronheiser, J.; Korevaar, B.; Sulima, O.; Rand, J. (2007), Silicon nanowire solar cells, *Appl. Phys. Lett.* Vol. 91, pp. 233117

Tsakalakos, L.; Balsh, J.; Fronheiser, J.; Shih, M.; LeBoeuf, S.; Pietrzykowski, M.; Codella, P.; Korevaar, B.; Sulima, O.; Rand, J.; Davuluru, A. & Rapol, U. (2007a), Strong broadband optical absorption in silicon nanowire films, *Journal of Nanophotonics*, Vol. 1, p. 013552

Tsu, R. & Babic, D. (1994) Doping of a quantum dot. *Appl. Phys. Lett.*, Vol. 64, pp. 1806–1808.

Uchiyama, H.; Nemoto, Y.; Dhamrin, M. & Kamisako, K. (2010),fabrication and evaluation of silicon nanowire solar cells, *Proceedings of 25th European Photovoltaic Solar Cell Energy Conference*, Spain, September 6-10, pp. 700-702.

Vo, T.; Williamson, A. & Galli, G. (2006), First principles simulations of the structural and electronic properties of silicon nanowires, *Phys. Rev. B.*, Vol. 74, pp. 045116.

Voz, C.; Peiró, D.; Bertomeu, J.; Soler, D.; Fonrodona, M. & Andreu, J. (2000), Optimisation of doped microcrystalline silicon films deposited at very low temperatures by hot-wire CVD, *Materials Science and Engineering B*, Vol. 69-70, pp. 278-283.

Wacker, A. (2002), Semiconductor superlattices: a model system for nonlinear transport, *Physics Reports*, Vol. 357, pp. 1-111.

Wang, X.; Pey, K. L.; Yip, C. H.; Fitzgerald, E. A. &Antoniadis, D. A. (2010), Vertically arrayed Si nanowire/nanorod-based core-shell p-n junction solar cells, *J. Appl. Phys.*, Vol. 108, pp. 124303.

Wang, X.; Pittet, P.; Gentil, P.; Noë, P. & Lévy-Clément, C. (2010a), Silicon nanowire arrays using colloidal crystal lithography and metal-assisted etching, *Proceedings of 25th European Photovoltaic Solar Cell Energy Conference*, Spain, September 6-10, pp. 191-194.

Wu, Y.; Cui, Y.; Huynh, L.; Barrelet, C.; Bell, D. & Lieber, C. (2004), Controlled growth and structures of molecular-scale silicon nanowires,.Vol. 4, pp. 433-436.

Yan, J.; Yang, L. & Chou, M. (2007), Size and orientation dependence in the electronic properties of silicon nanowires, *Phys. Rev. B.*, Vol. 76, pp. 115319.

Yang, M.; Cho, K.; Jhe, J.; Seo, S.; Shin, J.; Kim, K. & Moon, D. (2004) Effect of nitride passivation on the visible photoluminescence from Si-nanocrystals, *Appl. Phys. Lett.*, Vol. 85, pp. 3408.

Yao, D.; Zhang, G. & Li, B. (2008), A Universal Expression of Band Gap for Silicon Nanowires of Different Cross-Section Geometries, *Nano Lett.* Vol. 8, pp. 4557-4561.

Zacharias, M.; Heitmann, J.; Scholz, R.; Kahler, U.; Schmidt, M & Bläsing, J. (2002), Size controlled highly luminescent nanocrystals: A SiO/SiO2 superlattice approach, *Appl. Phys. Lett.*, Vol. 80, p. 661.

Zhang, R. Q.; Lifshitz, Y.; Ma, D. D. D.; Zhao, Y. L.; Frauenheim, Th.; Lee, S. T. & Tong S. Y., (2005) Structures and energetics of hydrogen-terminated silicon nanowire surfaces, *J Chem Phys*, Vol. 123, pp. 144703.

Zheng, G.; Lu, W.; Jin, S. & Lieber, C.M. (2004), Synthesis and Fabrication of High-Performance n-Type Silicon Nanowire Transistors, *Adv. Mater*. Vol. 16, pp. 1890-1893.

Zhong, Z.; Yang C. & Lieber, C. (2007) Chapter 5, in *Nanosilicon* (ed. By V. Kumar), Elsevier.

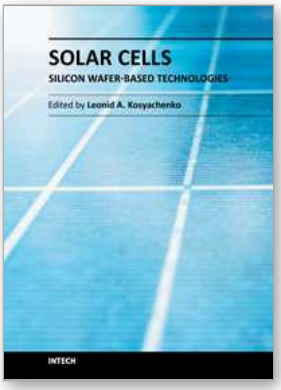

Solar Cells - Silicon Wafer-Based Technologies

Edited by Prof. Leonid A. Kosyachenko

ISBN 978-953-307-747-5
Hard cover, 364 pages
Publisher InTech
Published online 02, November, 2011
Published in print edition November, 2011

The third book of four-volume edition of 'Solar Cells' is devoted to solar cells based on silicon wafers, i.e., the main material used in today's photovoltaics. The volume includes the chapters that present new results of research aimed to improve efficiency, to reduce consumption of materials and to lower cost of wafer-based silicon solar cells as well as new methods of research and testing of the devices. Light trapping design in c-Si and mc-Si solar cells, solar-energy conversion as a function of the geometric-concentration factor, design criteria for spacecraft solar arrays are considered in several chapters. A system for the micrometric characterization of solar cells, for identifying the electrical parameters of PV solar generators, a new model for extracting the physical parameters of solar cells, LBIC method for characterization of solar cells, non-idealities in the I-V characteristic of the PV generators are discussed in other chapters of the volume.

InTech Europe
University Campus STeP Ri
Slavka Krautzeka 83/A
51000 Rijeka, Croatia
Phone: +385 (51) 770 447
Fax: +385 (51) 686 166
www.intechopen.com

InTech China
Unit 405, Office Block, Hotel Equatorial Shanghai
No.65, Yan An Road (West), Shanghai, 200040, China
中国上海市延安西路65号上海国际贵都大饭店办公楼405单元
Phone: +86-21-62489820
Fax: +86-21-62489821